Source Regions of the Interplanetary Magnetic Field and Variability in Heavy-Ion Elemental Composition in Gradual Solar Energetic Particle Events

Yuan-Kuen Ko[1], Allan J. Tylka[2], Chee K. Ng[3], Yi-Ming Wang[1], and William F. Dietrich[4]

yko@ssd5.nrl.navy.mil

ABSTRACT

Gradual solar energetic particle (SEP) events are those in which ions are accelerated to their observed energies by interactions with a shock driven by a fast coronal mass-ejection (CME). Previous studies have shown that much of the observed event-to-event variability can be understood in terms of shock speed and evolution in the shock-normal angle. But an equally important factor, particularly for the elemental composition, is the origin of the suprathermal seed particles upon which the shock acts. To tackle this issue, we (1) use observed solar-wind speed, magnetograms, and the PFSS model to map the Sun-L1 interplanetary magnetic field (IMF) line back to its source region on the Sun at the time of the SEP observations; and (2) then look for correlation between SEP composition (as measured by Wind and ACE at $\sim$2-30 MeV/nucleon) and characteristics of the identified IMF-source regions. The study is based on 24 SEP events, identified as a statistically-significant increase in $\sim$20 MeV protons and occurring in 1998 and 2003-2006, when the rate of newly-emergent solar magnetic flux and CMEs was lower than in solar-maximum years and the field-line tracing is therefore more likely

[1]Code 7680, Space Science Division, Naval Research Laboratory, Washington, DC 20375, USA

[2]Code 672, NASA Goddard Space Flight Center, Greenbelt, MD 20771, USA

[3]College of Science, George Mason Univesity, Fairfax, VA 22030, USA

[4]Praxis, Inc., Alexandria, VA 22303, USA

to be successful. We find that the gradual SEP Fe/O is correlated with the field strength at the IMF-source, with the largest enhancements occurring when the footpoint field is strong, due to the nearby presence of an active region. In these cases, other elemental ratios show a strong charge-to-mass (q/M) ordering, at least on average, similar to that found in impulsive events. These results lead us to suggest that magnetic reconnection in footpoint regions near active regions bias the heavy-ion composition of suprathermal seed ions by processes qualitatively similar to those that produce larger heavy-ion enhancements in impulsive SEP events. To address potential technical concerns about our analysis, we also discuss efforts to exclude impulsive SEP events from our event sample.

Subject headings: Sun: particle emission — Sun: abundances — Sun: heliosphere — Sun: solar wind — Sun: coronal mass ejections (CMEs) — Sun: flares — Physical data and processes: acceleration of particles — Physical data and processes: shock waves

1. Introduction

Coronal and interplanetary shocks driven by fact coronal mass ejections (CMEs) produce large gradual solar energetic particle (SEP) events, as evidenced by a large and continuously growing body of work, encompassing both observations (e.g., Kahler et al. 1978; Cane et al. 1988; Reames 1999, 2013; Tylka et al. 2005; Cliver & Ling 2007; Rouillard et al. 2011, 2012) and successful modeling efforts (e.g., Ng et al. 1999, 2001, 2003, 2012; Ng & Reames 2008; Zank et al. 2000, 2006; Li et al. 2003, 2005; Lee 2005, 2007; Tylka & Lee 2006; Sandroos & Vainio 2007, 2009). Intrinsic in this picture is the notion that SEPs observed upstream of the shock should reflect not only characteristics of the shock itself, but also characteristics of the environment in which the shock operates. In particular, the shock expands and crosses many magnetic field lines, which can emerge from different source regions on the Sun. Since the time-scale required for cross-field diffusion is long compared to the Sun-Earth transit time of >MeV/nucleon particles (Chollet & Giacalone 2011; Reames 2013), SEPs subsequently observed on those field lines should retain some signature of these

source regions.

Given this shock scenario, it might seem reasonable to expect some correlation between SEP and solar wind (SW) characteristics. Kahler & Reames (2003), for example, suggested that SEP production might be less prolific in fast SW streams compared to slow SW streams: both the MHD fast-mode speeds and the SW flow speeds are higher and therefore less favorable for shock acceleration in fast SW streams. Moreover, if ions in the suprathermal tails are the preferred SEP seed population (Mason et al. 1999; Desai et al. 2006; Tylka & Lee 2006; Lee 2007), then the weaker tails observed in fast SW regions (Gloeckler 2003) should further reduce SEP production in these regions.

But in a series of studies, none of these expectations was realized. Kahler (2004) compared SEP events in fast and slow SW regions, as identified by the O^{+7}/O^{+6} ratios; he found that the distribution of peak intensities of 20 MeV protons in fast and slow SW streams were the same. Kahler (2005, 2008) also found no dependence of any SEP-event timescale, such as rise times or durations, on SW stream type. Kahler et al. (2009) pursued this hypothesis by comparing elemental abundance ratios, energy-spectral indices, and ion intensities between SEP intervals within fast and slow SW streams, which were also identified by the thermal SW O^{+7}/O^{+6} ratios. Again, the results were negative, with no significant differences between SEPs in the two different types of SW streams.

In hindsight, perhaps these null results should not be surprising. Figure 1 plots O^{+7}/O^{+6} and the SW Fe/O abundance ratios versus SW helium speed in the non-interplanetary-CME (non-ICME) SW during years 2004-2006, using level-2, 2-hr averages measured by the Solar Wind Ion Composition Spectrometer (SWICS; Gloeckler et al. 1998) on the Advanced Composition Explorer (ACE). Also shown are histograms for these quantities in typical slow and fast SW speed regimes. Although the well-known anti-correlation between O^{+7}/O^{+6} and speed of the SW is evident, the range of scatter in O^{+7}/O^{+6} at any given SW speed is nearly an order of magnitude. In addition, even though the slow-SW Fe/O ratio (often used as indicator for First Ionization Potential (FIP) bias) is among the largest, there is a significant overlap in Fe/O between the fast and slow SW. It is therefore not surprising that categorizing by slow and fast SW (as defined either by SW speed or O^{+7}/O^{+6} ratio) fails to reveal any patterns in SEP variability – even if such correlations were to

exist.

Thus, it seems clear, that searching for correlations between SEP and SW characteristics requires a more subtle approach than comparing them as observed here at 1 AU. For this study, we adopt a different tactic: we first use the observed SW speed to map the Sun-L1 interplanetary magnetic field (IMF) line back to its source region on the Sun at the time of SEP observations. We then look for correlations between SEP composition and characteristics of the identified IMF-source regions. Our approach is motivated by two considerations. First, several lines of evidence suggest that suprathemal ions have a significant advantage over thermal ions when it comes to being efficiently accelerated by shocks (Mason et al. 1999; Desai et al. 2006; Tylka & Lee 2006; Lee 2007). Reconnection processes (Drake et al. 2009; Knizhnik et al. 2011) that occur at the IMF-source regions are one potentially promising source of suprathermal ions.

The second consideration involves how these suprathermals would encounter the shock. This is illustrated in Figure 2. The left cartoon shows that, before the CME eruption, open flux tubes (i.e., IMF) originate from different source regions, illustrated here as being either an isolated coronal hole (CH; blue lines) or a CH adjacent to an active region (AR, i.e., a strong-field region, red lines). After the CME eruption (right cartoon), the CME-driven shock will accelerate the seed particles in these flux tubes to high energies. Note that in this picture, seed particles upstream of the CME shock are characteristic of the source region *before* the eruption, even if the shock, field-line distortion, and/or reconnection subsequently change the particle properties in the downstream region. Moreover, any reconnection and reconfiguration that occurs in the wake of the CME launch will not destroy the validity of the magnetic traceback aimed at determining the solar origin of plasma and suprathermals that departed the Sun before the CME eruption. Therefore, the measured SEPs before the ICME arrives in-situ still reflect the seed particles that were present in the flux tubes before the CME occurred. *If suprathemal ions produced in various IMF-source regions are indeed different, these differences will be reflected in the SEPs.*

In a first-pass of the analysis, we qualitatively characterize the identified IMF-source regions according to the proximity of the Sun-L1 magnetic field-line's footpoint to an active region. These classifications, however, can be considered somewhat subjective, at least for a few of the events in our sample. We therefore make a second-

pass analysis in which the source region of the Sun-L1 field line is quantitatively characterized by the strength of the local photospheric magnetic field.

We begin this study by focusing on SEP measurements at 5-10 MeV/nucleon. A nearly identical energy range (at 5-12 MeV/nucleon) has been used previously to define the widely-cited average SEP abundance ratios that characterize gradual and impulsive SEP events (Reames 1995). This energy range is also measured with unsurpassed statistical precision by the powerful Low Energy Matrix Telescope (LEMT) in the Energetic Particle Acceleration, Composition, and Transport (EPACT) instrument package (von Rosenvinge et al. 1995) on Wind, which we use in this study. We will then use other LEMT channels to extend the study down to $\sim$2.5 MeV/nucleon. We also use data from the Solar Isotope Spectrometer (SIS; Stone et al. 1998a) on ACE to examine higher energies. In particular, for our selected time-intervals, ACE/SIS generally yielded statistical meaningful Fe/O measurements up to $\sim$30 MeV/nucleon. However, we restrict the present study to ions above 2.5 MeV/nucleon, so that the time required to traverse the nominal 1.2 AU Parker spiral pathlength from Sun to Earth is less than $\sim$2 hours, thereby avoiding potential complications that may arise for lower-energy particles with longer transit times.

We also begin by focusing on Fe/O, which is the most variable elemental ratio among well-measured SEP heavy-ion ratios. However, we also examine C/O, Ne/O, Mg/O, Si/O, S/O, Ar/O, and Ca/O. We omit He/O from the present study due to significant, unresolved instrument-to-instrument discrepancies that we have frequently encountered.

We describe our methodology for selecting SEP events and for identifying their corresponding magnetic-field source regions in Section 2. We also show examples of events that motivated this study. We present our detailed results on elemental composition, using the full event sample, in Section 3. Section 4 discusses our results and their implications for the origin of SEP event-to-event variability. Finally, an appendix discusses efforts taken to ensure that our event sample is not contaminated with impulsive events, in which a CME-driven shock is *not* responsible for promoting particles to their observed energies.

2. SEP Intervals and IMF Source Region Characterization

We began our study with the SEP event list used in Kahler et al. (2009), covering the years of 1998-2006. These events were identified on the basis of a statistically significant increase in the ∼20 MeV proton intensity observed by the Alpha-Proton-Electron (APE-B) particle telescope (von Rosenvinge et al. 1995) in the EPACT instrument-package on Wind. This telescope has lower background levels than the energetic particle instrument on the Geostationary Operational Environment Satellite (GOES; Onsager et al. 1996) and thus provides events over a larger range of sizes. By focusing on comparatively high proton energies, the selection discriminates against the more numerous impulsive SEP events, which are inherently proton-poor and rarely extend to such energies. We eliminated periods when the spacecraft were possibly within an ICME by examining the solar-wind magnetic, plasma, and ion-composition signatures. We also cross-checked our list with the ICME lists in existing literature (Lepri et al. 2001; Reinard 2008; Richardson & Cane 2010). In order to ensure meaningful measurements of SEP abundance ratios, we further required that the hourly-averaged ∼3 MeV/nucleon oxygen intensity reported by Wind/EPACT/LEMT exceed 10^{-4}/cm^2-sr-s-MeV/nucleon. This threshold eliminates periods in which anomalous cosmic rays, with typical oxygen intensities of 10^{-5}/cm^2-sr-s-MeV/nucleon (Reames & McDonald 2003), might significantly contaminate the measurements. In this study, we concentrate on events in 1998 and 2003-2006: the comparatively low rate of newly-emergent solar magnetic-flux and CMEs in these years make the magnetic field-line tracing more likely to be reliable. These initial selection criteria yielded 29 SEP events.

For each one-hour interval during the SEP events, we next traced the IMF observed at L1 back to the Sun and identified its source location. Using solar-wind speed measurements from the Solar Wind Electron Proton Alpha Monitor (SWEPAM; McComas et al. 1998) instrument on ACE[1], we assumed radial expansion and constant speed for each observed SW "parcel", so as to trace the SW plasma (and the asso-

---

[1]We compared simultaneous SW-speed measurements from SWEPAM and from the Solar Wind Experiment (SWE; Ogilvie et al. 1995) on Wind. For the time periods we examined, the SW speeds from the two spacecraft typically agreed to within less than 4%.

ciated IMF) ballistically from L1 to 2.5 $R_\odot$ (the source surface[2]). We then traced the magnetic field line from 2.5 $R_\odot$ to 1.0 $R_\odot$ using the potential-field source-surface (PFSS) model (Schatten et al. 1969), as implemented by Wang & Sheeley (1992) using radial photospheric magnetic maps from the Mt. Wilson Observatory[3] (MWO) with 5 degree resolution in longitude and latitude. That is, for a given SW parcel detected at L1 at a given time (tagged by Carrington rotation number and longitude), we found the corresponding Carrington rotation number/longitude/latitude at the solar surface. This position is equivalently the IMF-source location, i.e. the footpoint of the open magnetic field line that connected the Sun to L1 at the time of the SEP measurements. The solar structures around this location could then be conveniently identified using the Solar and Heliospheric Observatory (SOHO) Extreme-ultraviolet Imaging Telescope (EIT; Delaboudiniere et al. 1995) images, the Michelson Doppler Imager (MDI; Scherrer et al. 1995) full-disk magnetograms, and the synoptic maps constructed from these data. When SOHO data were not available, we used Yohkoh Soft X-ray Telescope (SXT; Tsuneta et al. 1991) or Transition Region and Coronal Explorer (TRACE; Handy et al. 1999) full-Sun mosaic images, and the synoptic maps from NSO Kitt Peak magnetograms.

It is perhaps worth noting that using the PFSS model is sometimes controversial even though, in practical terms, there are no other models that can identify the origin of IMF lines with much better accuracy (see Riley et al. 2006). This cautionary attitude is not unreasonable, given that reliability of the PFSS calculations is potentially affected by a number of factors (e.g. Neugebauer et al. 1998; Schrijver & DeRosa 2003; MacNeice et al. 2011), including the model's intrinsic assumptions and details of any specific implementation (such as corrections for line profile saturation, treatment of the polar fields, and the choice of input magnetograms, which may vary significantly from one observatory to another). Since the PFSS calculations start from synoptic maps of the photospheric magnetic field that are accumulated over $\sim$27 days, newly-emergent magnetic flux that is not properly represented in the

---

[2]In coronal magnetic-field models, the 'source surface' corresponds to the radial distance above which magnetic field lines are considered to be "open", thereby providing paths along which particles can escape from the corona into interplanetary space.

[3]The photospheric map from the National Solar Observatory (NSO) at Kitt Peak was used for Carrington Rotation 1935 due to gaps in the Mt. Wilson data.

maps can also adversely affect the accuracy of the field-line tracing. Moreover, the impact of these factors can vary from event to event, so that the accuracy of the PFSS calculations is not aways the same.

Nevertheless, the PFSS model has proven very successful in identifying the open-field regions at the Sun and the large-scale heliospheric structures such as magnetic sectors (e.g. Neugebauer et al. 1998, 2002; Wang & Sheeley 2006; Jian et al. 2009; Lee et al. 2009). More stringent tests of the PFSS model have come from mapping studies of impulsive SEP events (Nitta et al. 2006; Wang et al. 2006; Nitta & DeRosa 2008; Rust et al. 2008; MacNeice et al. 2011). Generally, these studies have found angular separations between the observed flare site and the PFSS-identified footpoint that disagree on average by $\sim$30 degrees, with a large spread among individual cases. However, impulsive SEP events are short-lived phenomena that originate in a compact region. Calculating the footpoint of an impulsive SEP event may therefore require a very precise description of a particular transient state of the coronal magnetic field. By contrast, in this study we are dealing with energetic particles generated by a shock over a broad expanse of field lines and over an extended time period. The PFSS model, in spite of its shortcomings, may well suffice to determine the dominant IMF-source in these circumstances. It is therefore best to judge the efficacy of the PFSS model in this study by the results: if the model does indeed elucidate a significant organization of the gradual-event variability, it is demonstrably adequate to the task.

One direct check of the PFSS result is to see if the magnetic polarity of the inferred source location agrees with that observed at L1 (e.g., Neugebauer et al. 1998, 2002; Rust et al. 2008). For this purpose, we used data from the Magnetic Field Experiment (Smith et al. 1998) on ACE. This consistency requirement removed only three SEP intervals from our study, leaving 26 events in our sample. This "26 out of 29" success ratio in the field polarity is *prima facie* evidence for the reliability of the field-tracing method.

As already noted, basing our initial event selection on $\sim$20 MeV protons discriminated against impulsive SEP events. At this point in the analysis, some unusually large and energetic impulsive events might still be in our sample. As detailed in the Appendix, we therefore next examined the abundance ratios of ^{3}He/^{4}He, trans-Fe ions to oxygen, and electrons-to-protons (e/p) to identify events that may be im-

pulsive rather than gradual. This examination resulted in the rejection of two more events. For the remaining 24 events, we compared the distributions of Fe/O and e/p ratios to expectations for pure samples of impulsive and gradual events. As further detailed in the Appendix, we then fit our distributions to a linear combination of these two templates. This analysis indicated that the best estimate for residual impulsive-event contamination in our sample was 6% with uncertainty ranges of +9% and -5%, consistent with zero.

Table 1 lists the remaining 24 events, including the start and end times of time intervals used in further study of composition characteristics. Note that these intervals do not necessarily encompass the whole SEP event due to our imposed intensity threshold on ∼3 MeV/nucleon oxygen, magnetic-polarity mismatches, and/or our exclusion of ICMEs. Table 1 also gives details about the flare and CME identifed with the source of the SEPs[4]. Table 2 lists: (1) the Carrington Rotation number/longitude/latitude of the flare/CME source location; (2) this same information for the IMF-source location on the source surface at 2.5 $R_\odot$; (3) the angular separation between the flare-CME source and the IMF-source location at 2.5 $R_\odot$; (4) the IMF-source location at 1 $R_\odot$ at the start of the SEP study-interval and (5) at the end of the SEP study interval; (6) the latitude and longitude of the IMF-source location at 1 $R_\odot$ at the start of the study interval; (7) and the angular separation between the flare/CME source and the IMF-source at 1 $R_\odot$ at the start of the SEP study-interval. The final two columns of Table 2 give: (8) the NOAA AR (if any) that is located within 15 degrees of the IMF-source region, and (9) a label that classifies the IMF-source region (see Section 3.1). One SEP event (#20) was broken into two time intervals, when the field-line mapping switched from one IMF-source region to another. At the source surface, all of the IMF-footpoints lie in the western hemisphere at the times of the SEP events, as expected. At 1 $R_\odot$, all of the IMF footpoint locations are also in the western hemisphere, with longitudes ranging between W17 and W89. In comparison, the flare/CME source longitudes (given in Table 1) range over nearly the whole Sun, from E134 to W157.

Figures 3 and 4 illustrate some of the data used in our analysis. Each figure

---

[4]Based on information from http://www.solarmonitor.org, http://www.lmsal.com/solarsoft/latest_events/, and/or http://cdaw.gsfc.nasa.gov/CME_list/ unless noted otherwise.

shows two events, one in each column. In each column, the top panel shows the synoptic Carrington map of the Sun from SOHO/EIT $\lambda 195$ emission. In these maps, ARs are seen as areas of bright EUV emission. The second panel in each column shows the same synoptic map based on SOHO/MDI radial magnetograms. In the MDI maps, ARs appear as bipolar or multi-polar field, with white/black patches representing strong positive/negative fields. Note that the apparent strength of the ARs in the Carrington maps, which are collages accumulated over 27-days, is not necessarily the same as at the time of the SEP event. In both Carrington maps, a yellow circle marks the source region of the CME/flare that produced the SEPs, plotted with a nominal 15-degree-radius. The white (gray) 15-degree-radius circle on the EIT map marks the IMF footpoint location at the start (end) of the time interval in Table 1, as determined from our PFSS calculations[5]. The amount of systematic eastward drift of the footpoint over the duration of the event varies from event to event, depending on the coronal field configuration and how the field lines spread out. Over the course of the event, the IMF-footpoint location drifts on average by ∼6 degrees in longitude; but for four of the events in our sample, the longitude drift is 10-20 degrees. The white oval on the MDI map shows the union of the footpoint circles during the SEP interval. We see that the IMF footpoint locations are not necessarily at the flare/CME source, some of which can be more than 90 degrees apart (see Table 2).

The third panel in each column displays the Carrington map of contemporaneous radial photospheric magnetic fields from Mt. Wilson[6], along with results of PFSS field-line mappings. The radial component of the photospheric field is represented by gray scale contours, with white (black) denoting positive- (negative-) polarity flux with strengths above 20 G. The yellow and green areas are the footpoint areas of open field lines of positive and negative polarity, respectively, as traced back by the PFSS model from a grid of points on the source surface at 2.5 $R_\odot$. The horizontal row of red diamonds represents the ecliptic plane's intersection with the source surface. Red lines connect the source-surface longitudes to the corresponding photospheric source of the IMF, as determined by the PFSS calculation.

---

[5]Justification for use of this size for the footpoint circle will be presented in Section 3.4.

[6]For events #1 and #2, the photospheric fields come from National Solar Observatory (NSO) at Kitt Peak, due to a Mt. Wilson data gap.

In the photospheric map in the left-column of Figure 3, the identified footpoint region shows an example in which field lines originate in a photospheric region of limited longitudinal extent but expand so as to provide the open field over several tens of degrees of longitude on the source surface. In the right column, on the other hand, inferred footpoint locations are spread over a range of longitudes within the coronal hole whose longitudinal extent is comparable to that of the field lines at the source surface. Thus, in both of these cases – and in general – we find that a particular coronal hole provides the origin of the Sun-L1 field lines for the entire multi-day duration of a gradual SEP event.

The bottom panel in each column shows SEP data from Wind/EPACT, with the time profile of hourly-averaged intensities of 19-21 MeV protons and 5-10 MeV/nucleon oxygen and iron ions in the upper plot and the hourly-averaged Fe/O, Si/O and C/O ratios at 5-10 MeV/nucleon in the lower plots. A solid vertical line marks the flare/CME launch time, whose solar location and speed, respectively, are noted. Dashed vertical lines mark the start (S) and end (E) of time interval used in this study. Horizontal lines in the lower panels indicate the average ratios for gradual SEPs at 5-12 MeV/nucleon, as determined by Reames (1995).

Characteristics of SEP events are governed by a number of factors, such as the speed of the shock-driving CME (Reames 2000) and the longitude of the CME source region (Cane et al. 1988; Reames et al. 1996). But the large degree of multi-faceted event-to-event variation suggests that there are also other factors that have not yet been elucidated. To discover these other factors in event-to-event variability, it is helpful to compare events in which CME-speed and CME source-region longitudes are similar. Given our small event sample, we can find pairs of events that match only roughly in these quantities. Thus, Figure 3 compares two events (#2 and #3) with very fast CMEs ($\sim$2300 and $\sim$1900 km/s, respectively) launched from regions behind the west limb (estimated at W102 and W157, respectively). The very fast CMEs and comparatively remote flare locations make it very likely that shock-accelerated particles would overwhelm any direct flare contribution, even if a direct flare contribution were allowed by the magnetic topology, which is questionable (Reames 2002). Figure 4 compares two more events (#11 and #15), this time with lower CME speeds ($\sim$1000 and $\sim$1200 km/s, respectively) and erupting from regions near the center of the solar disk (W16 and W01, respectively).

In comparing the events in the left and right columns of Figures 3 and 4, we note two striking differences:

(1) *Nature of the IMF Footpoint Region*: Close inspection of the EIT/ MDI maps and the PFSS results show that the footpoints of the events in the left-hand columns are located in close proximity to an active region; the events in the right-hand columns, by contrast, show the footpoint inside a coronal hole, without a nearby active region. We henceforth denote these two classifications of the IMF-source region as an "active" coronal hole (A-CH) and a "quiet" coronal hole (Q-CH), respectively. (The operational criteria for classifying the type of footpoint region will be described in more detail in Section 3.) A quantitative distinction between these two types of footpoint regions is presented in Figure 5, which displays histograms of the magnitude of the radial magnetic field in the $\sim 10^5$ MDI pixels within the footpoint areas near the time of the start of the SEP event. (Details are given in Section 3.4 below.) As expected, high field values are much more prevalent in the IMF-source regions that have been classified as "A-CH".

(2) *Heavy-Ion Composition*: The bottom panels of Figures 3 and 4 display striking compositional difference between the events in the left- and right-hand columns. Specifically, in both figures the left-hand events (with "A-CH" IMF-source regions) show enhancements in the heavy ion ratios compared to the gradual-SEP averages (Reames 1995). On the other hand, the events in the right-hand columns (with "Q-CH" IMF-source regions) have heavy-ion ratios that are below the gradual-SEP averages. For example, in Figure 3, the A-CH event (#2, left) has Fe/O values that are more than twice the gradual-SEP average of 0.134 ± 0.004, whereas the Q-CH event (#3, right) has Fe/O that averages only $\sim$5% of the gradual-SEP value. Event #2 also shows higher Si/O ratios; and a close examination of interval-integrated quantities shows the Event #2 also has a higher O/C (that is, lower C/O) ratio than Event #3. These compositional differences between these two events persist over the entire durations, with very little time-dependence in the hourly-averaged ratios.

The two events in Figure 4 show similar differences in Fe/O and Si/O, albeit with less extreme values. The elemental ratios in these events also show some transient structure near the start of the event, when particle intensities are low. This initial temporal structure is likely the result of rigidity-dependent interplanetary transport, which can arise when an ion's charge-to-mass ratio is different from that of oxygen

(Tylka et al. 1999; Ng et al. 1999, 2003; Mason et al. 2006; Tylka et al. 2012). Although these transport distortions are seen in some of our events, they are present for too few hours to compromise our general characterization of the elemental composition. (See Figure 11, below.) Moreover, given the low-intensities associated with these transport distortions, this initial variability has little effect on event-integrated ratios[7].

Extreme values of SEP Fe/O sometimes reflect strong spectral differences between the O and Fe ions (Tylka et al. 2005, 2006). Figure 6 compares the event-averaged energy spectra for O and Fe ions at $\sim$2-40 MeV/nucleon for the four events in Figures 3 and 4. Contamination from anomalous cosmic rays and Galactic cosmic rays have been subtracted from the spectra, using the methods described in Tylka et al. (2006) and the contemporaneous 27-day averaged "quiet-time" rates from SIS and the Cosmic Ray Isotope Spectrometer (CRIS; Stone et al. 1998b) on ACE. In all four events, the oxygen spectrum is reasonably well described by a single or double power-law over this entire energy range, without any hardening at high energies that might suggest more than one acceleration mechanism operating in the event (Tylka et al. 2005). In all four events, the Fe spectrum has a somewhat more complicated shape, which is not surprising in that Fe ions typically have a much broader range of charge-to-mass ratios (Tylka et al. 2000, 2001, 2005). The Fe/O ratios thus exhibit some modest energy dependence (see Table 3). Nevertheless, Figure 6 clearly shows that spectral shapes do not drive the difference in Fe/O among the events. Compared to the events with an A-CH IMF-source region (left column), the events from Q-CH IMF-source regions (right column) are depleted in Fe relative to O over this whole energy range. This fact suggests that the difference in Fe/O between the two events likely derives not from the acceleration mechanism, but rather, from the composition of the seed population upon which the acceleration mechanism acts.

It is also perhaps worth noting that in these two pairs of events, in which we have roughly matched CME-speed and CME-source longitude, the events with A-CH IMF-source regions show significantly higher oxygen intensities. This is what would be expected for shock acceleration operating in the presence of an enhanced

---

[7]The event-integrated ratio of Fe/O, for example, is determined by separately averaging the Fe and O intensities over the duration of the event and then calculating the ratio of these average intensities.

suprathermal seed population. However, given the residual differences in CME speeds and CME-source longitudes, no strong conclusions can be drawn on this point.

Figure 7 shows two further examples of events with A-CH IMF-source regions. Event #14, (left panel, and which is discussed in more detail in the Appendix) has the highest Fe/O values in our study (but still well-below the impulsive-SEP average of 1.078 ± 0.046 (Reames 1995)). Fe/O in Event #12 (right panel) is only slightly enhanced over gradual-SEP average.

Finally, Figure 8 shows two more examples of events with Q-CH IMF-source regions. The right column shows events #16 and #17, in which two CMEs successively erupted from the same source region while the footpoint location remained in the same area. In both events, Fe/O is suppressed, although the hour-by-hour variation in the Fe/O ratio also exhibits transport distortions.

Figures 9 shows histograms of the footpoint magnetic field values for the four events in Figures 7 and 8. The difference between A-CH and Q-CH IMF-source regions is apparent, just as in Figure 5. Figure 10 shows the event-averaged O and Fe spectra for the events in Figures 7 and 8. In these events, Fe/O shows somewhat stronger energy-dependence than the events in Figure 6. But once again, the qualitative distinction in the Fe/O ratios between the A-CH (left column) and Q-CH (right column) IMF-source regions is clear over the whole energy range.

3.   SEP Heavy-Ion Composition and the Source Region of the IMF

The eight events shown in Figures 3-10 suggest that compositional differences among gradual SEP events can be related to the character of the IMF-source region, either A-CH or Q-CH. More specifically, high field values are much more prevalent in the A-CH IMF-source regions. Any magnetic reconnection within areas containing such large, complex, and dynamic magnetic fields might reasonably be expected to be much more effective in producing suprathermal ions that could subsequently become seeds for shock acceleration. Moreover, if these reconnection processes are similar to those that produce impulsive SEP events (Drake et al. 2009; Knizhnik et al. 2011), the suprathermals may have impulsive-like enhancements in heavy ions (Reames 2000; Reames & Ng 2004; Mason et al. 2004). We now explore that notion

more fully by examining the complete event sample, using not only hourly-averaged abundance ratios, but also interval-integrated ratios and ensemble-averages of events in the two classes.

The objective of this study is to search for factors in the IMF-source regions that correlate with the variation in SEP heavy-ion elemental composition. It is well-known that the elemental composition at the Sun varies among different structures. For example, solar spectroscopic observations found that the First Ionization Potential (FIP) bias (defined as the density ratio of a low-FIP element (FIP below ∼10 eV) to a high-FIP element (FIP above ∼ 10 eV) relative to their photospheric ratio) is around 2-4 or higher in ARs and is <2 in CHs (e.g. Raymond et al. 2001 and references within). This result, which is based on thermal plasma, points to a possibility that suprathermal particles in the ambient corona may also have different elemental composition among different solar structures. These different suprathermal compositions would serve as an initial condition for acceleration into SEPs by CME-driven shocks.

When the IMF footpoint locations are identified as described in the previous section, one obvious way to characterize them is to examine the solar structure in the vicinity of the footpoints. The basic AR and CH structures are usually obvious when relying on solar images, e.g. in EUV or X-rays, to distinguish them in various coronal emission lines or wavelength bands. However, the structures can be quite different in relative intensity and spatial extent, depending on which spectral lines from which ions dominate the emission recorded in that particular image. A more robust quantity for characterization purposes is the photospheric magnetic field. Indeed, the constantly-evolving solar magnetic field underlies all the dynamic phenomena of the Sun, including evolution of the solar structures, coronal heating, and transients. Different structures have their own magnetic characteristics. For example, ARs are the strongest magnetic regions and the most variable in their dynamical range, whereas CHs have weaker magnetic field with one dominant polarity. Therefore we also examine the solar structures in the vicinity of the footpoints based on magnetograms to find out if different solar structures are in any way related to different levels of heavy-ion enhancements.

3.1.   Relationship to Solar Structures

We group the IMF footpoint structures associated with their respective SEP time-intervals into two categories: (1) "active coronal-hole" (A-CH) IMF-sources if the L1-to-Sun field lines trace back to the close proximity of an AR (whether the CH is visible or not) and (2) "quiet coronal-hole" (Q-CH) IMF-sources if the field lines trace back to a CH without an AR in its vicinity. We identify ARs in the solar images using the list compiled in the NOAA/USAF Active Region Summary[8]. We define 'close proximity' and 'vicinity' as being within a 15-degree-radius circle around the predicted footpoint location at the start of the SEP interval. (See Section 3.4 for justification of this choice.) In addition, an AR exhibits itself as localized strong magnetic field as can be seen in the MDI magnetogram images/synoptic maps, and bright in the coronal ($\sim$million degrees) emission such as in the EIT λ195 images (Figures 3, 4, 7, 8). Note that judging whether an AR is within the range of the circle from an emission image is somewhat subjective since the range of brightness in an AR can be quite different when seen from different emission sources. By contrast, using the magnetogram is more robust in defining the spatial extent of an AR. The result of this categorization is listed in Table 2. Some A-CH IMF-sources were the same active region where the SEP event's associated flare/CME occurred (denoted in the last column of Table 2 as 'AR0'); others were a different active region ('AR1'). The Q-CH IMF-sources included both equatorial/low-latitude coronal holes ('EqCH') and low-latitude extension of polar coronal holes ('PCH').

The top panels of Figure 11 plot hourly-averaged Wind/EPACT SEP Fe/O and C/O ratios at 5-10 MeV/nucleon from our 25 SEP intervals versus simultaneous thermal SW Fe/O and C/O measurements from ACE/SWICS. The plot shows only those data points that are significant at the 2-sigma level or larger. The data are color-coded according to either 'A-CH' (red triangles) or 'Q-CH' (blue crosses) IMF-sources. While there is clearly no correlation between SEP Fe/O and SW Fe/O, the larger SEP Fe/O are preferentially associated with A-CH IMF-sources, while smaller SEP Fe/O ratios are preferentially associated with Q-CH IMF-sources. The middle panels of Figure 11 show the histograms of the SEP Fe/O and C/O values, again color-coded according to the type of the IMF-source. There is substantial overlap in

---

[8]As given at www.solarmonitor.org

the histograms, but the preference for Fe/O enhancements from A-CH IMF-sources is clear. By comparison, as shown in the bottom panels, there is no difference between the histograms of SW Fe/O ratios for A-CH and Q-CH IMF-sources. It is interesting to see that SEP Fe/O values >0.20 are almost exclusively associated with A-CH IMF-sources (thus strong magnetic field regions); such high values are rarely observed in the non-ICME, thermal solar wind. On the other hand, the SEP Fe/O values for Q-CH IMF-sources extend toward values below the photospheric value of 0.065 ± 0.004 (Asplund et al. 2009).

For comparison, the green dash-dot and purple dashed lines in top and middle panels of Figure 11 mark average values observed in impulsive and gradual SEP events at 5-12 MeV/nucleon, respectively (Reames 1995). Except for a small fraction of the hourly values, often coming from the onsets of events when intensities are low, the SEP Fe/O values here are well below the impulsive-SEP average. This fact in itself is strong evidence against any substantial contribution from impulsive events in our sample. Instead, our distribution of SEP Fe/O straddles the gradual-SEP average, with Q-CH IMF-sources mostly below the gradual-SEP average and A-CH IMF-sources mostly above.

A long-standing puzzle has been the difference in the average C/O between SEPs $(0.465 \pm 0.009$; Reames 1995) and thermal SW $(0.68 \pm 0.07$; Bochsler 2007). As shown in Figure 11, this difference is also seen in the events of our study. Figure 11 also shows that the lowest SEP C/O values (or, equivalently, the highest O/C values) come primarily from A-CH IMF-sources. By contrast, A-CH and Q-CH IMF-sources show virtually no difference in SW C/O values.

3.2. Energy-Dependence of the Fe/O Ratio

Fe/O measurements at other energies are given in Table 3. The top panel of Figure 12 is a scatter plot of Fe/O vs. energy for the individual intervals, but with abscissae slightly displaced by varying amounts, so that individual events (distinguished by symbol and color) can be seen. The bottom panel shows the energy dependence of the ensemble averages, that is, the averages of the interval-integrated ratios for time-intervals associated with A-CHs or with Q-CHs. Also shown are power-law fits to the energy-dependence in the two cases. The Fe/O ratio for the Q-CH IMF-sources,

at least on average, has no significant energy dependence and agrees with the photospheric Fe/O value. For A-CH IMF-sources, the average Fe/O ratio is higher than the Q-CH average by a factor of $\sim$4. The A-CH Fe/O shows a modest increase with energy, suggesting a tendency for Fe spectra to be slightly harder than oxygen spectra in these events. Overall, however, the compositional distinction between the two types of source regions is clear over the entire energy range of $\sim$2-30 MeV/nucleon.

3.3.   Additional Elemental Ratios

Table 4 reports elemental ratios at 5-10 MeV/nucleon for species other than Fe. Figure 13 plots the interval-integrated ratios relative to oxygen, with different symbols representing different intervals. The symbols are also color-coded according to the identified type of IMF-source region (red for A-CH, blue for Q-CH). One event (#10, which is discussed further below) is an outlier in these distributions with an unusually low Fe/O value for an A-CH IMF-source region. Otherwise, compared to Q-CH IMF-source regions, A-CH IMF-source regions tend to show enhancements in the heavier species in all of the element ratios. There is a large degree of overlap between the A-CH and Q-CH distributions for the lighter species. However, as the element grows heavier, the bifurcation between A-CH and Q-CH IMF-sources becomes clearer.

Figure 14 displays ensemble-averages. The ratios are shown for both SEPs at 5-10 MeV/nucleon (left panel) and for the simultaneously-observed solar-wind at L1 (right panel). Also plotted in the SEP panel are the average values reported for gradual and impulsive SEP events at nearly the same energy (5-12 MeV/nucleon; Reames 1995). Among the noteworthy features:

1. In all of these SEP ratios, the heavier ion is more abundant for A-CH IMF-source regions than for Q-CH IMF-source regions.

2. In the SEPs, the degree of bifurcation between A-CH and Q-CH regions becomes larger as the the ion becomes heavier. In fact, as shown in Figure 15, the ratio of the A-CH to Q-CH values is reasonably well-organized by the charge-to-mass ($<q>/M$) ratio, where $<q>$ values are the gradual-SEP averages

measured by Luhn et al. (1984) at $\sim$0.5-2.5 MeV/nucleon[9]. The $< q > /M$-ordering shown in Figure 15 is reminiscent of what is observed in impulsive SEP events (Reames 2000; Reames & Ng 2004, Mason et al. 2004), suggesting that the same physical processes governing composition in those events are also affecting the suprathermal seed particles for gradual SEP events.

3. Except for Si and S, the Reames (1995) gradual-SEP averages lie between our A-CH and Q-CH SEP averages. Since our results reflect event-to-event variation among gradual events, this is generally what we would expect to find. However, for Si and S, the Reames (1995) gradual-SEP averages are slightly higher than the average values we have found in our survey; it is unclear why this is so.

4. In all cases except C/O, our A-CH averages are well-below the impulsive-SEP average from Reames (1995). (Average C/O values are nearly identical for gradual and impulsive SEP events.)

5. The Mg/Ne ratio provides a measure of the FIP step in heavy-ion populations. For the Q-CH and A-CH enembles, the average Mg/Ne ratios are 1.38 $\pm$ 0.09 and 1.16 $\pm$ 0.16, respectively. The difference between these values is not statistically significant. Thus, there is no evidence that FIP-effect plays a significant role in generating the observed differences in SEPs for A-CH and Q-CH IMF-source regions.

6. Compared to the SEPs, the solar-wind abundance ratios show very little bifurcation between the A-CH and Q-CH IMF-source regions. This is not surprising in that the distributions of solar-wind speeds for both types of source regions are broad and similar among the intervals in our study. (Differences in SW composition are most clearly observed when comparing the extremes of the SW speed distribution.)

---

[9]For Ar and Ca, which were not measured by Luhn et al. (1984), we use $< q >= 10.1$ and $< q >= 10.6$, respectively, as expected for a 2 MK source plasma (Bryans et al. 2009). For the mass of Ar, we use an average value of M_{Ar}=36.3 based on isotopic-composition measurements from SEPs (Leske et al. 2007) and from meteorites (Lodders 2008).

7. There is no clear relationship between elemental ratios in the SEPs and in the SW. Compared to their SW averages, Ne/O and Si/O are suppressed. The average Mg/O ratios, on the other hand, are enhanced in SEPs relative to the SW values; and the average SW Fe/O values lie between our SEP values. This lack of correspondence between SEP and SW elemental ratios is consistent with previous studies (e.g., Desai et al. 2006; Mewaldt et al. 2007), which also disfavored the thermal solar-wind as the primary seed-population for heavy-ions in gradual SEPs.

3.4.   Correlations with Photospheric Magnetic Field Strength

The results shown above imply that the SEP Fe/O is generally larger if the open field lines that transport the SEPs are rooted near a region with strong magnetic field. To investigate this in a quantitative way, we now search for correlations between measured magnetic field properties at the IMF footpoint regions and the SEP heavy-ion composition. For this purpose, we use the synoptic maps built from the SOHO/MDI Level-1.8 data to obtain the *radial* magnetic field flux density (B) at and around the IMF footpoints. These synoptic maps are provided at a given disk meridian of choice (e.g. central meridian, 15W, 30W, 45W, 60W, etc) and have 3600 x 1080 bins with the axes linear in longitude and sine-latitude. See the MDI website (http://sun.stanford.edu/synop) for details regarding how these synoptic maps were constructed. We chose the disk meridian map closest to the solar longitude of the predicted IMF footpoint region at the time of the event.

Quantitative characterization of the IMF footpoint region requires consideration of two factors. First, as already noted, the predicted footpoint locations generally drift over the course of the SEP interval. Second, the *a priori* uncertainty is unknown for our IMF traceback results, which probably also varies from event to event. To address these two factors, we proceed as follows: first, we determine the footpoint location at the start and stop of the SEP time interval and then draw a line between these two points. Around each point on this line, we draw a circle of a specified angular radius. (For example, the angular radius is 15 degrees in Figures 3, 4, 7, 8.) We then evaluate the average magnitude of of B (that is, $< |B| >$) using the pixels within the union of these circles. We repeated such calculations for angular

radii of 5 to 50 degrees in increments of 5 degrees. For large angular radii, the included area may extend beyond the map. In this case, we stitch the synoptic map of the neighboring Carrington Rotation so as to take into account the part of the area outside of the primary map. We also exclude bins at latitudes greater than 60 degrees since the radial magnetic field (which is derived from the measured line-of-sight field) may not be reliable there. Note that Events 5 and 6 are not included in these calculations because there were no MDI data due to an interruption in SOHO operations.

Figure 16 shows scatter plots of the interval-integrated Fe/O at 5-10 MeV/nucleon versus $< |B| >$ for six sizes of the averaging circle. Also shown are the correlation fits, which in all cases demonstrate a tendency for Fe/O to increase with $< |B| >$. Noted on each plot is the Pearson correlation coefficient. Since we have 23 SEP intervals, a correlation coefficient greater than 0.525 is significant at the $>99\%$ confidence level.

The analysis shown in Figure 16 was also repeated for energy bins above and below our best-measured interval at 5-10 MeV/nucleon. Figure 17 summarizes the dependence of the correlation coefficient on averaging radius for these three energy bins. In all cases, when the circle is too small, the correlation becomes insignificant, presumably because the circle often misses the relevant magnetic region. The correlations also become insignificant when the averaging-circles become too large and therefore "wash-out" the relevant magnetic structure. At all three energies, the correlations are significant at the $>95\%$ confidence level when the averaging radius is $\sim$15-30 degrees. We take these results as a measure of the typical uncertainty in our magnetic-field traceback method and use of the PFSS. Indeed, if our traceback were not generally reliable at this level, it is difficult to imagine how such significant correlations could be generated accidentally with an otherwise unrelated observable, such as SEP Fe/O.

One particular outlier is noteworthy in Figure 16: Event #10 has the lowest Fe/O among our events with A-CH footpoints. In fact, the Fe/O in Event #10 is highly suppressed, which at first glance is inconsistent with the pattern we have seen heretofore. However, the footpoint region for Event #10 just barely clipped the edge of an active region (NOAA AR 10331), which was both weak and decaying prior to the SEP event. In order to maintain the internal consistency of our analysis, we will

continue to classify Event #10 as having an A-CH footpoint. However, this may not really have been the case.

Figure 16 suggests that the *magnitude* of the photospheric magnetic field strength is a factor that affects the SEP heavy-ion composition[10]. It seems likely that this correlation arises through the intermediary of the suprathermal seed particles, whose composition is affected by the photospheric magnetic field, either directly or indirectly. This would be conceptually similar to those solar observations that found higher FIP bias in higher B-field structure (Raymond et al. 2001). Figure 16 is also plotted with IMF-source categorization, with A-CH and Q-CH as filled-red and open-blue triangles, respectively. There is some overlap between the A-CH and Q-CH populations in Figure 16, which, at least in part, is probably due to the uncertainties in determining the footpoint magnetic field strength. Nevertheless, we see that for footpoint-uncertainty circles where the correlation is statistically significant, most A-CH IMF-sources have both larger $< |B| >$ and higher SEP Fe/O ratio than the Q-CH IMF-sources.

3.5. Fe/O versus Angular Separation from the Flare/CME Source

The angular separation between the flare/CME source and the magnetic footpoint of the SEP observer is a factor that influences various aspects of event-to-event variability, such as the shapes of SEP time-intensity profiles (Cane et al. 1988; Reames et al. 1996). These angular separations are given in column 8 of Table 2. Figure 18 plots the SEP Fe/O at 5-10 MeV/nucleon versus this angular separation. The datapoints are color-coded according to their classification as Q-CH (blue) or A-CH (red). In addition, the size of the symbol indicates the value of $< |B| >$ as averaged over a 15-degree circle around the IMF footpoint. The event numbers (from Table 1) are also noted on the figure.

All of the events in which the angular separation is less than 15 degrees are classified as A-CH by definition; as expected, they all show larger than average Fe/O and higher $< |B| >$ values. For angular separations between 20 and 100 degrees, the

---

[10]We also examined plots of Fe/O versus the average signed B (that is, $| < B > |$) but found no significant correlations in those cases.

numbers of A-CH and Q-CH events are equal. (As discussed previously, Event #10 is an outlier, probably with an incorrect A-CH classification.) For angular separations beyond 100 degrees, all five intervals are Q-CH, with lower than average Fe/O and comparatively small $< |B| >$. There is no *a priori* reason why events with large angular separations between the IMF-footpoint and the flare/CME source should have weak $< |B| >$ and concomitantly low Fe/O. It may be relevant, however, to note that four of these five intervals occurred after June 2005, by which time the number of active regions on the Sun had fallen by more than half compared to the rest of the time period used in this study. Many of the coronal holes in the late phase of the solar cycle also tend to be larger and farther away from active regions, thus making Q-CH IMF-sources more likely (Wang 2012).

As an alternative to our hypothesis, it might be suggested that higher Fe/O values result from cross-field transport of flare-accelerated ions from the flare/CME source. This scenario would require the flare and CME-driven shock to have produced comparable fluences of ions, at least in the ~5-10 MeV/nucleon energy range. This scenario would also require a faster time-scale for cross-field diffusion than has been deduced by other recent studies (Chollet & Giacalone 2011; Reames 2013). If feasible, this alternative would presumably imply an anti-correlation between Fe/O and the angular separation. This anti-correlation[11] is indeed seen in Figure 18, albeit with a correlation coefficient that is somewhat smaller than those seen in Figures 16 and 17 for 15-30 degree $|B|$-averaging circles. Nevertheless, the correlation in Figure 18 is significant at the ~95% confidence level. Thus, the alternative hypothesis, which attributes the event-to-event variability in Fe/O to angular distance from the flare site – rather than strength of the footpoint magnetic field – cannot be excluded by this study alone. Other considerations, as well as a larger event sample, may help to distinguish between the hypotheses.

---

[11]An earlier study of Fe/O at 0.6-1.0 MeV/nucleon showed a much weaker and statistically insignificant anti-correlation (Mason et al. 1984, Figure 4). This is true even if the data in our Figure 18 are restricted to angular separations less than 110 degrees, just as in the earlier study.

4. Discussion

We have discovered that elemental composition in gradual SEP events is governed, at least in part, by the strength of the photospheric magnetic field around the footpoints of the IMF along which the SEPs are transported. That is, the SEP elemental composition differs depending on whether the solar footpoint of the IMF is in a quiet coronal hole (Q-CH, without a nearby active region) or in an active coronal hole (A-CH, with a nearby active region). These differences are most apparent for Fe/O (Figures 11, 13, 16). The differences are not an artifact of time-dependence in Fe/O (i.e., Figures 3, 4). The difference in Fe/O is seen over the whole energy range survey here, $\sim$2-30 MeV/nucleon (Figures 6, 10, 12) and thus are not simply a spectral effect reflecting acceleration biases. More generally, SEPs from an A-CH IMF-source demonstrate an ordering by charge-to-mass ($< q >$/M) ratio, less pronounced but analogous to that seen in impulsive-SEP events (Figure 15). To our knowledge, this study is the first successful attempt to relate gradual-SEP event-to-event compositional variation to differences in the solar IMF-source regions.

We tentatively interpret our results as follows: *the composition of suprathermals available for shock acceleration depends on the photospheric magnetic field where suprathermals are generated and thus is different for A-CH and Q-CH IMF-sources.* In the A-CH IMF-sources, suprathermals may be generated by reconnection processes similar to those that produce impulsive SEP events, which also require the presence of an active region (Mason et al. 2009). In Q-CH IMF-sources with surrounding weak magnetic field, however, the associated loops are characteristic of quiet-Sun structures, and the preferential enhancements in heavy ions apparently are not as large.

Our interpretation is consistent with other lines of evidence on reconnection activity and its potential impact on suprathermal populations. Active regions are locations of complex and strong magnetic field where constant field emergence and footpoint motions tend to cause magnetic reconnections among field lines. Quasi-separatrix layers (QSLs) formed in the AR's complex magnetic topology are found to be the locations of ubiquitous outflows in ARs observed by the EUV Imaging Spectrometer (EIS) on Hinode, indicating that magnetic reconnection occurs quasi-continually along the QSLs and some can release particles into the solar wind (e.g. Baker et al. 2009, van Driel-Gesztelyi et al. 2012, Démoulin et al. 2013). X-

ray observations by the Reuven Ramaty High Energy Solar Spectroscopic Imager (RHESSI) have shown that microflares, which are signs of small-energy-scale magnetic reconnections, are seen only in active region locations; these microflares also occur more frequently during solar-maximum years (Christe et al. 2008). Furthermore, Kocharov et al. (2008) reported extended periods of enhanced suprathermal ^{3}He in the slow solar wind that originated from near-AR footpoints. Taken together, these observations suggest that these microflares do indeed produce suprathermals with systematic heavy-ion enhancements analogous to those seen in impulsive-SEP events. This scenario, if correct, would provide a natural explanation for our results. More generally, Dayeh et al. (2009) showed that Fe/O and ^{3}He/^{4}He ratios in quiet-time suprathermals are enhanced during solar maximum years as compared to solar minimum years. These results may also be related to higher levels of reconnection in active years, either from microflares or as remnants from preceding SEP events.

The differences in SEP composition from the A-CH and Q-CH IMF-sources presumably reflect how environmental factors in the footpoint region (such as magnetic structure, flux emergence rate, field strength, the density and velocity distributions of electrons and ions) affect the production and nature of the local suprathermal-ion populations. Theoretical efforts on magnetic reconnection – aimed at understanding how the intensity, energy-distribution, and composition of suprathermals depend on these factors – can also help to clarify the viability of our interpretation. Should we expect, for example, larger enhancements in suprathermal Fe/O when the B field is stronger?

Our results show that the SEP elemental composition is positively correlated with the average *unsigned* photospheric magnetic field (that is, $<|B|>$) around the associated IMF footpoints. However, as seen in Figure 16, there is significant spread among the Fe/O values for a given value of $<|B|>$. Further studies are needed to investigate other factors that can contribute to this variation. One possible factor is the spatial resolution of the magnetic field maps. The AR and CH structures at the Sun consist of magnetic field of both polarities, but with more unbalanced flux from one polarity in the CH. The fact that there is no correlation with the average of *signed* magnetic field (that is, $|<B>|$) can be understood by the fact that most opposite-polarity fluxes just cancel with each other when averaged over a large area. This in turn points to the possibility that the correlation scale shown in Figure 16 might change quantitatively with the spatial resolution of the input magnetic field

maps. The MDI maps we used appear to be sufficient for the investigations reported here. But higher spatial resolution maps may 'stretch' the $<|B|>$ scale to larger values (because of less mutual-cancellation of large fields in smaller spatial pixels), perhaps thereby improving the correlation in Figure 16.

This initial study used SEP events observed during comparatively quiet solar-active years of Solar Cycle 23, in 1998 and 2003-2006. During these years, ARs were relatively sparsely distributed and large low-latitude coronal holes were frequently present. We purposely avoided the years of peak activity in 1999-2002, during which the rate of flux emergence in the form of new active regions was higher. The primary reason for this was to increase the likely reliability of our field-line tracing. In particular, on the timescale of a solar rotation, a potentially significant source of error in the field-line tracing is new flux emergence: if a new active region emerges well after the central-meridian date for its longitude, it will not be properly represented in the synoptic photospheric map[12]. Consequently, it may prove difficult to extend this study to years of higher activity, at least when using synoptic field maps accumulated over a full solar rotation. Extension of the techniques developed here to more active periods may very well require new sources of photospheric maps, accumulated by multiple spacecraft observing simultaneously from widely-spaced solar longitudes.

High-energy heavy ions can damage electronics on spacecraft (Tylka et al. 1996), although penetration of typical shielding requires ion energies much higher than those considered here. At present, it is believed that solar ions heavier than helium are a negligible radiation hazard for astronauts. However, this is a tentative conclusion that may be revised as the biological effects of so-called "HZE ions" (with high atomic number and energy) becomes better understood (van Hoften et al. 2008). Our findings may therefore have potential space-weather application in predicting the heavy-ion content of SEP events.

Our results may also be useful for constraining and validating coronal/heliospheric magnetic field models. For example, if an event-integrated SEP Fe/O is greater than 0.20 (see Figure 16), the associated IMF is likely to be rooted near an AR with strong magnetic field. Similarly, if an event-integrated SEP Fe/O is less than 0.06, the IMF

---

[12]The emergence rate of very small bipoles (ephemeral regions) does not vary much over the solar cycle, and, in any case, does not affect the large-scale field and open flux.

is likely to be rooted in an isolated coronal hole without an AR nearby. The SEP data can therefore be used to identify cases in which the field-line tracing is incorrect and thereby lead to refinements of coronal/heliospheric magnetic field models and field-line mapping techniques. In turn, more reliable predictions for the solar-wind footpoint locations at the Sun will advance efforts to understand the origin(s) and formation of the solar-wind.

As previously mentioned, there is justifiable concern about using the PFSS model to map the interplanetary magnetic field back to its photospheric source-region, primarily because of the uncertainties and limitations of the model. These uncertainties and limitations include: (1) the corona, especially in ARs, is not current free; (2) the Carrington map used as model input is not realistic enough for the ever-changing conditions at the Sun, such as emerging magnetic flux and CMEs; and (3) the IMF structure between the Sun and the in-situ instrument is not really known. In fact, all current coronal/heliospheric magnetic field models that are used to trace the IMF back to the Sun share similar shortcomings (see MacNeice et al. 2011 for detailed evaluations).

In this study, we have applied the PFSS model to gradual SEP events, which has not been done before. We find that the PFSS model, in spite of these well-known shortcomings, is generally accurate enough for our purposes: (1) in $\sim$90% of the events in this study, the field-line mapping matched the SW field polarity at 1 AU and the inferred polarity at the footpoint; (2) our identification of A-CH and Q-CH IMF-sources revealed a striking distinction in the SEP composition (Figures 11-15); (3) the PFSS mappings also led to rather robust results on the correlation between the SEP Fe/O and the strength of the footpoint magnetic field (Figures 16 and 17). Given the size of our event sample (24 events, 25 intervals), it is difficult to imagine how such robust results would arise if the PFSS model were fundamentally unreliable in identifying the IMF sources in gradual SEP events.

At present, it should be possible to extend this work using SEP observations from ACE and Wind at L1 and from the STEREO spacecraft in 2011-2013, years which have thus far also exhibited a relatively low level of solar activity. In the future, it should also be possible to repeat these studies with measurements closer to the Sun from Solar Probe Plus and Solar Orbiter, thereby reducing some of the systematic uncertainties. If the results reported here are confirmed by further studies, they will

be an important advance in our understanding of how the two fundamental particle acceleration mechanisms – magnetic reconnection and shock-acceleration – combine to explain event-to-event variability in gradual SEP events.

5.   Appendix

As discussed in Section 2, field-line mapping successfully identified the footpoint of the Sun-L1 magnetic-field line for all or part of 26 SEP events. These events are listed in Table A1, along with observables found useful in previous efforts at classifying events as either "gradual" (that is, in which a CME-driven shock promotes particles to their observed energies) or "impulsive" (in which particles derive their observed energies from magnetic reconnection, such as that associated with a flare). Column 1 of Table A1 identifies the events with the same numbers used in Table 1. However, Table A1 also contains two additional events (in bold font, labeled I1 and I2, and starting on 2004 October 30 and 2005 May 6, respectively) which, for the reasons discussed below, were rejected from our study as impulsive SEP events.

Table A1 contains event-integrated ratios (1) for Fe/O from Wind/LEMT at 3.2-10 MeV/nucleon (2) trans-Fe ratios for atomic number $Z > 34$ relative to oxygen in this same energy interval, also from Wind/LEMT; and (3) ^{3}He/^{4}He ratio at 0.32-0.64 MeV/nucleon from the Ultra Low Energy Isotope Spectrometer (ULEIS; Mason et al. 1998) on ACE. In order to maximize statistical precision, the abundance ratios were calculated using the entire event interval given in Table A1, rather than just sub-intervals during which field-line tracing could be carried out. (For the lower-

energy ACE/ULEIS data, the event-integration typically started ~4-8 hours later, depending on background levels preceding the event.) The Fe/O and Z($>$34)/O ratios in Table A1 are normalized to their nominal coronal values, 0.134 and 2.66 $\times$ 10^{-5}, respectively, as given by Reames (1995, 2000).

With regard to the ion ratios, we note the following:

(1) All of the *normalized* Fe/O values are well below 8.04 $\pm$ 0.41, which is the average value observed in purely impulsive SEP events (Reames 1995). The highest normalized Fe/O values, at ~5 times the nominal value, were found in Events I1, I2 and #14. (Event #14 will be discussed in more detail below.)

(2) Only Events I1 and I2 have significant trans-Fe enhancements, at several tens times the coronal value. Such values are found in impulsive SEP events (Reames 2000; Mason et al. 2004; Reames & Ng 2004). Event #14 may also be enhanced in trans-Fe elements; but to within large statistical uncertainties, it is also consistent with nominal coronal composition. Within uncertainties, trans-Fe ratios in 13 other events are also consistent with the nominal coronal value to within less than a factor of three. In the remaining ten events, the trans-Fe ratio is an upper limit $\geq$9, which alone is too high to permit any conclusion about the particle-acceleration mechanism.

(3) The ACE/ULEIS ^{3}He/^{4}He ratios were extracted from online data obtained from the ACE website[13]. For all but two events Table A1 reports a 95% confidence-level upper limit that is less than 3 percent[14]. None of the events attained the $>$10% ratio used to identify impulsive events in many earlier studies. These upper limits do not preclude impulsive acceleration, but they are also consistent with the more modest ^{3}He/^{4}He ratios often observed in gradual events when particles previously energized in flares are available in the shock's seed population (Mason et al. 1999, 2002). Only Event I1 has an enhancement in ^{3}He/^{4}He that is sufficiently large and well-determined (6.0 $\pm$ 0.2%) to be taken as conclusive evidence for particle acceleration at reconnection site(s). Event #14 has an usually high upper-limit of

---

[13]http://www.srl.caltech.edu/ACE/

[14]Background limitations in the online data, which often can be ameliorated by careful analysis of pulse-height data not accessible by us, suggest that ratios less than a few percent derived from online data should generally be interpreted as upper limits.

<5.8%. But as shown in Figure A1, Event #14 erupted during the declining phase of earlier events. The timelines of ^{4}He and Fe show an increase associated with this new event, but an increase is difficult to discern in the ^{3}He timeline; hence, the upper limit.[15]

Thus, among the events in Table A1, only Event I1 has all three of the heavy-ion signatures associated with impulsive SEP events. Event I2 has enhanced Fe/O and (Z>34)/O but only an upper limit on ^{3}He/^{4}He that is not inconsistent with an impulsive event.

For a closer examination, Figure A2 shows electron and selected ion time-intensity profiles for Events I1 and I2. The time structure is most clearly revealed in the electron data. In particular, both events show a series of distinct injections of near-relativistic electrons. In both events, these electron injections are temporally associated with soft x-ray flares, which are listed in Table A2. All of these flares are "impulsive" (that is, with durations less than $\sim$20 minutes) and emanate from a single active region in each event. Electrons events like these are generally recognized as signatures of magnetic reconnection that can also produce impulsive heavy-ion enhancements (Reames et al. 1985; Wang et al. 2012). Moreover, our field-line mapping for the 14 electron events in Table A2 traced back to solar longitudes that were on average within $\sim$28-degrees of the reported flare locations, consistent with earlier studies of impulsive SEP events (MacNiece et al. 2011).

Table A2 also lists the speed, estimated launch times, and width of CMEs associated with these SXR flares. Most of these CME have speeds at 200-700 km/s and hence slower than those typically found in association with gradual events. Such comparatively slow CMEs are unlikely to drive shocks that can accelerate ions to to $\sim$MeV/nucleon energies (Reames 2000, Kahler 2001, Gopalswamy et al. 2004). These speeds are comparable, however, to the speed of CMEs sometimes observed (perhaps coincidentally) in association with impulsive SEP events (Yashiro et al. 2004).

For Event I2, two of the associated CMEs have speeds exceeding 1100 km/s. Both of these CMEs are somewhat narrow (109 and 129 degrees) compared to most

---

[15]The upper limit on ^{3}He/^{4}He in Event #8 also includes ^{3}He from the declining phase of a preceding impulsive event.

SEP-producing CMEs, a factor that might limit their effectiveness as a particle accelerator (Kahler et al. 1999). With these speeds, we cannot be certain that the CME-driven shock did not also contribute to acceleration of some of the energetic particles. However, the observed trans-Fe enhancement favors acceleration at the reconnection site as the dominant source of the energetic heavy-ions in this event.

Taken together, these characteristics suggest that Events I1 and I2 are not gradual events, but rather, the product of a sequence of impulsive events. We have therefore omitted these two events from further analysis.

But what can we say about possible "residual" contamination from impulsive events in our event sample?

The bottom panel of Figure A3 shows the histogram of Fe/O values from the surviving 24 events in Table A1. This histogram is compared with two others. The top histogram is based on 71 very large gradual events from 1995 -May 2012, identified by requiring the GOES event-integrated fluence of >30 MeV protons to exceed 2×10^5 cm^{-2}-sr^{-1} (Tylka et al. 2005), thereby selecting the largest SEP events of this era. The middle histogram is derived from 172 impulsive SEP events in Cycle 23, identified by requiring that the ACE/ULEIS event-integrated ^{3}He/^{4}He ratio at 0.32-3.56 MeV/nucleon exceed 10%. Since ^{3}He/^{4}He and Fe/O enhancements are uncorrelated in impulsive SEP events (Mason et al. 1986; Reames et al. 1994), this selection criterion provides an unbiased survey of Fe/O variability in impulsive events.

The histogram for gradual events presents Fe/O at 3.2-10 MeV/nucleon, the same energy range used in Table A1. Comparisons at the same energy are important for gradual events, since Fe/O sometimes has a significant energy-dependence in these events (Tylka et al. 2002, 2005), most likely reflecting multiple components in the seed population, some of which are preferentially accelerated to higher energies (Tylka & Lee 2006; Sandroos & Vainio 2007, 2009) . For impulsive SEP events, on the other hand, Fe and O energy spectra are nearly identical in shape (Tylka et al. 2002; Mason et al. 2002; Wiedenbeck et al. 2010), so that the Fe/O ratio has essentially no energy dependence. The lower energy range of 0.32-0.64 MeV/nucleon used for Fe/O in the impulsive events, which was chosen so as to optimize statistical precision, is therefore not a concern when comparing to the distribution of Fe/O values in gradual events.

The similarity of the Fe/O histograms from our events and from the gradual events is clearly evident. The fitted means of the two histograms agree to within statistical uncertainty. To further quantify these comparisons, we take the distributions shown in the top and middle panels of Figure A3 as templates for the Fe/O distributions for gradual and impulsive events, respectively. We then fit the bottom panel (our events) to a linear combination of the two. That is, let x_i, y_i, and z_i be the fraction of events in histogram-bin i for gradual events, impulsive events, and our event sample, respectively. Let f, where $0 \leq f \leq 1$, be the fraction of events in our event sample that are impulsive. Thus,

$$z_i = (1 - f)x_i + fy_i. \tag{1}$$

We can find the value of f that best describes our event sample by minimizing the quantity

$$\chi^2 = \sum \frac{(z_i - (1 - f)x_i - fy_i)^2}{\sigma_i^2}. \tag{2}$$

where the sum runs from $i = 1$ to $i = N_{bins}$, where N_{bins} is the number of bins in the histogram in which at least one of x_i, y_i, or z_i is non-zero and

$$\sigma_i^2 = \sigma_{z,i}^2 + (1 - f)^2\sigma_{x,i}^2 + f^2\sigma_{y,i}^2 \tag{3}$$

and $\sigma_{x,i}$, $\sigma_{y,i}$, and $\sigma_{z,i}$ are the statisitical uncertainties on x_i, y_i, and z_i, calculated with Poisson error bars (Geherels 1986).

Figure A4 shows χ^2/ν, where $\nu = N_{bins} - 1$, plotted versus the impulsive fraction f. This result clearly disfavors a significant fraction of impulsive events in our data. In fact, the best-fit fraction of impulsive events among our sample is $2\ ^{+12}_{\ -2}$ %, consistent with zero.

In that the focus of this study is variability in SEP heavy-ion composition, it is also useful to have another means of distinguishing "gradual" and "impulsive" SEP events. Ramaty et al. (1980) showed that the gradual and impulsive particle acceleration mechanisms also differ in their relative effectiveness in accelerating protons

and electrons, with empirically-defined electron/proton (e/p) ratios generally much higher in impulsive events. Cliver & Ling (2007) revisited this notion with more recent and comprehensive particle data. In particular, they developed distinctions between impulsive and gradual events based on hourly-averaged peak intensities of electrons (from the Comprehensive Suprathermal and Energetic Particle Analyzer (COSTEP; Müller-Mellin et al. 1995) on SOHO) and protons (from GOES). The same quantities as used by Cliver & Ling are also reported[16] in Table A1, as well as the corresponding e/p ratio.

Cliver & Ling amalgamated SEP event lists from several earlier studies, none of which used the same event-selection criteria as our study. They identified a sample of impulsive SEP events on the basis of strong ^{3}He/^{4}He, Fe/O, and/or trans-Fe enhancements observed by Wind/LEMT. Cliver & Ling also compiled a sample of gradual events for which the associated flare in each case was at a comparatively remote solar longitude (specifically, east of W20 or behind the west limb) and thus unlikely to a have a significant direct flare-contribution.

Cliver & Ling found that none of the 41 impulsive events in their sample had peak-hourly GOES >10 MeV proton intensity above 3.0/cm^2-sr-s. Among the 59 gradual SEP events in the Cliver & Ling survey, however, proton intensities were above and below this value in roughly equal numbers. In our final event sample, the proton intensities are also distributed roughly equally above and below this value. Events I1 and I2 both have proton intensities less than this value. Note that proton intensity in Event #14 is nearly 20 times the upper limit reported for impulsive events by Cliver & Ling.

---

[16]GOES proton instruments are optimized for the study of the large SEP events that are potential space-weather hazards. Because of possible concern about the reliability of GOES measurements in relatively small events, we also estimated the >10 proton MeV intensity from power-law fits to the 8-25 and 25-63 MeV proton intensities reported by the COSTEP instrument on SOHO. Proton measurements from this instrument have much lower background levels than that of GOES. We found that the ratio of GOES to COSTEP values for the peak >10 MeV proton intensity ranged from 0.5 to 2.5, with an average GOES/COSTEP proton ratio of 1.3. We also cross-checked the SOHO/COSTEP electron intensity against measurements from the Electron, Proton, and Alpha Monitor (EPAM; Gold et al. 1998) on ACE, using the correlation relation given by Cliver & Ling in their equation (1). We found that ratio of COSTEP to EPAM values for the peak 0.25-0.70 MeV electron intensity ranged from 0.4 to 1.2, and with an average ratio of 0.8.

Cliver & Ling suggested that events for which their empirical e/p ratio exceeds ~1500 should generally be classified as "impulsive". Event I1 meets this criterion, with the second largest largest e/p ratio among the events in Table A1. However, Event #9 has an even larger e/p ratio (~4400). Figure A5 presents the hourly-averaged time-intensity profiles for electrons and protons (top panel), as well as Fe and O ions (bottom panel) in three different energy ranges, from ACE/ULEIS (0.32-0.64 MeV/nucleon), Wind/LEMT (3.2-10 MeV/nucleon), and ACE/SIS (~10-35 MeV/nucleon) for Event #9. There are no unusual features in the electron and proton timelines, such as a second injection of electrons, that might account for the high e/p ratio. Among the ions, the Fe intensity falls well below the O intensity in all three energy bins, except for the first ~5 hours of the event in ACE/ULEIS. (This initial, transient Fe/O enhancement is likely a transport effect (Ng et al. 1999; Tylka et al. 2012).) In fact, relative to the gradual-SEP average value, the event-integrated Fe/O ratios in these three energy ranges are 2.46 ± 0.05, 1.36 ± 0.10, and 1.30 ± 0.19, respectively. As seen in Table A1, trans-Fe and ^{3}He/^{4}He ratios are only upper limits. Thus, heavy-ion measurements provide no justification for classifying Event #9 as "impulsive". For this reason, we retain Event #9 in our analysis.

Cliver & Ling further found that the electron and proton intensities were strongly correlated in gradual events, but that the correlation was weaker in impulsive events. These correlations are shown in the top two panels of Figure A6. The bottom panel of Figure A6 shows this same correlation for our 24 events.

Also shown in each panel is the best least-squares correlation fit, along with the correlation coefficient and the fit parameters. The correlation fits are very different between the gradual (top) and impulsive (middle) panels. The correlation coefficients in both the Cliver & Ling gradual events and in our events are much higher than that of the impulsive events. To within the uncertainties on the fit parameters, the correlation for our events is identical to that from the Cliver & Ling gradual events.

Figure A7 compares histograms of the empirical e/p ratios from Cliver & Ling gradual and impulsive events and from our event sample. The gradual and impulsive histograms have significant overlap, so that it is generally not possible to classify an individual event on the basis of the e/p ratio alone. Nevertheless, the difference in the overall histograms is readily apparent. The histogram for our events is very similar to that of the Cliver & Ling gradual events, with fitted means that agree to

within a few percent.

Using the top two panels of Figure A7 as templates, we repeated the fitting exercise we applied above to the Fe/O distributions. For the e/p histograms, the fitted impulsive fraction among our events is $10\ ^{+14}\ _{-10}$ %, also consistent with zero. Combining these two independent determinations (that is, from Fe/O and e/p histograms), the fraction of impulsive events in our sample becomes $6\ ^{+9}\ _{-5}$ %, again consistent with zero. For comparison, if we add back into our analysis the two impulsive events I1 and I2, fits to the histograms yield an impulsive fraction of $12\ ^{+9}\ _{-8}$ %, consistent with the 2-out-of-26 ratio deduced from our detailed examination of the events in Table A1.

In summary, among the 24 events in our final event sample, 14 of them have magnetic footpoints close to active regions. *A priori* it might be reasonable to think that some of these events are exhibiting particles directly accelerated to their observed energies by magnetic reconnection, rather than by interaction with a shock. Except for the two events (I1 and I2) that were deleted from our analysis, examination of the (Z>34)/O, ^{3}He/^{4}He, and e/p ratios revealed no event with clear or consistent signatures of an impulsive origin. Moreover, the observed Fe/O and e/p distributions strongly reject any notion that a significant fraction of our events are impulsive in nature. We therefore conclude that the event-to-event composition variability seen in this study arises *not* from different energetic-particle acceleration mechanisms, but rather, from different processes in the production of the seed particles that feed into shocks.

Finally, as previously noted, Event #14 has the same Fe/O value as the two impulsive events we rejected from our study. The trans-Fe and ^{3}He/^{4}He ratios were inconclusive on the acceleration mechanism. We accepted this event as 'gradual" because of its comparatively large proton intensity. But why does this gradual event have an especially high Fe/O ratio?

Figure A8 takes another look at Event #14. Less than 3 hours before the launch of the CME (from a region behind the west limb), an impulsive M1.1 flare erupted from AR 10691, which was near the Sun-L1 footpoint and had previously caused the series of impulsive SEP events shown in the top panel of Figure A2. As shown in Figure A8, this M1.1 flare produced a detectable increase of ~0.5 MeV electrons observed by SOHO/COSTEP. If this flare were like the previous impulsive flares

from this active region, it likely produced suprathermal ions with impulsive-SEP-like abundance enhancements. These suprathermals would then have been available as seed particles for the CME-driven shock when the shock intercepted the Sun-L1 field line, thereby generating the observed compositional characteristics of this event.

REFERENCES

Asplund, M., Grevesse, N., Sauval, A. J., & Scott, P. 2009, ARAA, 47, 481

Baker, D., van Driel-Gesztelyi, L., Mandrini, C. H., Démoulin, P., & Murray, M. J. 2009, ApJ, 705, 926

Bryans, P., Landi, E., & Savin, D. W. 2009, ApJ, 691, 1540

Bochsler, P. 2007, A&AR 14, 1

Cane, H. V, Reames, D. V. & von Rosenvinge, T. 1988, J. Geophys. Res., 93, 9555

Christe, S., Hannah, I. G., Krucker, S., McTiernan, J., & Lin, R. P. 2008, ApJ, 677, 1385

Chollet, E. E. & Giacalone, J. 2011, ApJ, 728, 64

Cliver, E. W. & Ling, A. G. 2007, ApJ, 658, 1349

Dayeh, M. A., Desai, M. I., Dwyer, J. R., Rassoul, H. K., Mason, G. M., & Mazur, J. E. 2009, ApJ, 693, 1588

Delaboudiniere, J.-P., et al. 1995, Sol. Phys., 162, 291

Démoulin, P., Baker, D., Mandrini, C. H., & van Driel-Gesztelyi, L. 2013, Sol. Phys., 283, 341

Desai, M. I., Mason, G. M., Gold, R. E., Krimigis, S. M., Cohen, C. M. S., Mewaldt, R. A., Mazur, J. E., & Dwyer, J. R. 2006, ApJ, 649, 470

Drake, J. F., Cassak, P. A., Shay, M. A., Swisdak, M., & Quaaert, E. 2009, ApJ, 700, L16

Gehrels, N. 1986, ApJ, 303, 336

Gloeckler, G. 2003, in AIP Conf. Proc. 679, eds. M. Velli, R. Bruno, F. Malara, & B. Bucci, 583

Gloecker, G., et al. 1998, Space Sci. Rev., 86, 497

Gold, R. E., et al. 1998, Space Sci. Rev., 86, 541

Gopalswamy, N. 2003, Geophys. Res. Lett., 30, 8013

Gopalswamy, N., Yashiro, S., Krucker, S., Stenborg, G., & Howard, R. A. 2004, J. Geophys. Res., 109, DOI: 10.1029/2004JA010602

Handy, B. N., et al. 1999, Sol. Phys., 187, 229

Jian, L. K., Russell, C. T., Luhmann, J. G., Galvin, A. G., & MacNeice, P. J. 2009, Sol. Phys., 259, 345

Kahler, S. W. 2001, J. Geophys. Res., 106, 20947

Kahler, S. W. 2004, ApJ, 603, 330

Kahler, S. W. 2005, ApJ, 628, 1014

Kahler, S. W. 2008, J. Geophys. Res., 113, A11102

Kahler, S. W., & Reames, D. V. 2003, ApJ, 584, 1063

Kahler, S. W., Burkepile, J. T., and Reames, D. V. 1999, Proc. 26th ICRC (Salt Lake City), 6, 248

Kahler, S. W., Hildner E., van Hollebeke, M. A. I. 1978, Sol. Phys., 57, 429

Kahler, S. W., Tylka, A. J., & Reames, D. V. 2009, ApJ, 701, 561

Kocharov, L., Laivola, J., Mason, G. M., Didkovsky, L., & Judge, D. L. 2008, ApJS, 176, 497

Knizhnik, K., Swisdak, M., & Drake, J.F. 2011, ApJ, 743, L35

Lee, M. A. 2005, ApJS, 158, 38

Lee, M. A. 2007, Space Sci. Rev., 130, 221

Lee, C. O., Luhmann, J. G., Odstrcil, D., MacNeice, P. J., de Pater I., Riley, P., & Arge, C. N. 2009, Sol. Phys., 254, 155

Lepri, S. T., Zurbuchen, T. H., Fisk, L. A., Richardson, I. G., Cane, H. V., & Gloeckler, G. 2001, J. Geophys. Res., 106, 29231

Leske, R.A., Mewaldt, R.A., Cohen, C.M.S., Cumming, A.C., Stone, E.C., Wiedenbeck, M.E., & von Rosenvinge, T.T. 2007, Space Sci. Rev, 130, 195

Li, G., Zank, G. P., & Rice, W. K. M. 2003, J. Geophys. Res., 108, 1082

Li, G., & Zank, G. P. 2005, Geophys. Res. Lett., 32, L02101

Lodders, K. 2008, ApJ674, 607

Luhn, A. et al. 1984, Adv. Space Res., 4(2-3), 161

MacNeice, P., Elliott, B., & Acebal A. 2011, Space Weather, 9, S10003

Mason, G. M., Gloeckler, G., & Hovestadt, D. 1984, ApJ, 280, 902

Mason, G. M., et al. 1986, ApJ, 303, 849

Mason, G. M., et al. 1998, Space Sci. Rev., 86, 409

Mason, G. M., Mazur, J. E., & Dwyer, J. R. 1999, ApJ, 525, 133

Mason, G. M., et al. 2002, ApJ, 574, 1039

Mason, G. M., et al. 2004, ApJ, 606, 555

Mason, G. M., Desai, M. I., Cohen, C. M. S., Mewaldt, R. A., Stone, E. C., & Dwyer, J. R. 2006, ApJ, 647, 65

Mason, G. M.; Nitta, N. V.; Cohen, C. M. S.; & Wiedenbeck, M. E. 2009, ApJ, 700, L56

McComas, D. J., et al. 1998, Space Sci. Rev., 86, 563

Mewaldt, R. A. et al. 2007, Space Sci. Rev., 130, 207

Müller-Mellin, R. et al. 1995 Sol. Phys., 162, 483

Neugebauer, M. et al. 1998, J. Geophys. Res., 103, 14587

Neugebauer, M., Liewer, P. C., Smith, E. J., Skoug, R. M., & Zurbuchen, T. H. 2002, J. Geophys. Res., 107, 1488

Ng, C. K. & Reames, D. V. 2008, ApJ, 686, L123

Ng, C. K., Reames, D. V., & Tylka, A. J. 1999, Geophys. Res. Lett., 26, 2145

Ng, C. K., Reames, D. V., & Tylka, A. J. 2001, Proc. 27th Int. Cosmic Ray Conf. (Hamburg), 8, 3140

Ng, C. K., Reames, D. V., & Tylka, A. J. 2003, ApJ, 591, 461

Ng, C. K., Reames, D. V., & Tylka, A. J. 2012, AIP Conf. Proc., 1436, 212

Nitta, N. V., & DeRosa M. L. 2008, ApJ, 673, L207

Nitta, N. V., et al. 2006, ApJ, 650, 438.

Ogilvie, K. W., et al. 1995, Space Sci. Rev., 71, 55

Onsager, T., et al. 1996, Proc. SPIE, 2812, 281.

Ramaty, R. et al. 1980, in Solar Flares, ed. P. A. Sturrock (Boulder: Colorado Associated Univ. Press), 117

Raymond, J. C. et al. 2001, in Joint SOHO/ACE workshop "Solar and Galactic Composition". Edited by Robert F. Wimmer-Schweingruber. in AIP Conf. Proc. 598, 49

Reames, D. V. 1995, Adv. Space Res., 15, 41

Reames, D. V. 1999, Space Sci. Rev., 40, 413

Reames, D. V. 2000, AIP Conf. Proc., 516, 289

Reames, D. V. 2002, ApJ, 571, L63

Reames, D.V. 2013, Space Sci. Rev, DOI: 10.1007/s11214-013-9958-9

Reames, D. V. & McDonald, F. B. 2003, ApJ, 586, L99

Reames, D. V. & Ng, C. K. 2004, ApJ, 610, 510

Reames, D. V., Meyer, J. P. & von Rosenvinge, T. 1994, ApJS, 90, 649

Reames, D. V., Barbier, L.M., & Ng, C. K. 1996, ApJ466, 473

Reames, D. V., von Rosenvinge, T. T., & Lin, R. P. 1985 ApJ, 292, 716

Reinard, A. A. 2008, ApJ, 682, 1289

Richardson, I. G., & Cane, H. V. 2010, Sol. Phys., 264, 189

Riley, P., Linker, J. A., Mikić, Z., Lionello, R., Ledvina, S. A. & Luhmann, J. G. 2006, ApJ, 653, 1510

Rouillard, A.P., et al. 2011, ApJ, 735, 7

Rouillard, A.P., et al. 2012, ApJ, 752, 44

Rust, D. M., Haggerty, D. K., Georgoulis, M. K., Sheeley, N. R., Wang, Y.-M., DeRosa, M. L., & Schrijver, C. J. 2008, ApJ, 687, 635

Sandroos, A. & Vainio, R. 2007, ApJ, 662, L127

Sandroos, A. & Vainio, R. 2009, ApJS, 181., 183

Schatten, K. H., Wilcox, J. M., & Ness, N. F. 1969, Sol. Phys., 6, 442

Scherrer, P. H., et al. 1995, Sol. Phys., 162, 129

Schrijver, C. J. & DeRosa, M. L. 2003, Sol. Phys., 212, 165

Smith, C. W., et al. 1998, Space Sci. Rev., 86, 613

Stone, E. C., et al. 1998a, Space Sci. Rev., 86, 357

Stone, E. C., et al. 1998b, Space Sci. Rev., 86, 285

Tsuneta, S., et al. 1991, Sol. Phys., 136, 37

Tylka, A. J., Dietrich, W. F., Boberg, P. R., Smith, E. C., & Adams, J. H., Jr. 1996, IEEE Trans. Nucl. Sci. 43(6), 2758

Tylka, A. J., Reames, D. V., & Ng, C. K. 1999, Geophys. Res. Lett., 26, 2141

Tylka, A. J., Boberg, P. R., McGuire, R. E., Ng, C. K., & Reames, D. V. 2000, AIP Conference Proc. 528, Acceleration and Transport of Energetic Particles in the Heliosphere, ed. R. A. Mewaldt, J. R. Jokipii, M. A. Lee, E. Möbius, & T. H. Zurbuchen,(Melville: AIP), 147

Tylka, A. J., et al. 2001, ApJ, 558, L59

Tylka, A. J., Boberg, P. R., Cohen, C. M. S., Dietrich, W. F., Maclennan, C. G., Mason, G. M., Ng, C. K., & Reames, D. V. 2002, ApJ, 581, L119

Tylka, A. J., Cohen, C. M. S., Dietrich, W. F., Lee, M. A., Maclennan, C. G., Mewaldt, R. A., Ng, C. K., & Reames, D. V. 2005, ApJ, 625, 474

Tylka, A. J., Cohen, C. M. S., Dietrich, W. F., Lee, M. A., Maclennan, C. G., Mewaldt, R. A., Ng, C. K., & Reames, D. V. 2006, ApJS, 164, 536

Tylka, A. J., & Lee, M. A. 2006, ApJ, 646, 1319

Tylka, A. J., et al. 2012, Sol. Phys.,DOI: 10.1007/s11207-012-0064-z

van Driel-Gesztelyi, L. et al. 2012, Sol. Phys., 281, 237

van Hoften, J. D. A., et al. 2008, Managing Space Radiation Risk in the New Era of Space Exploration, The National Academies Press, (Washington DC), http://www.nap.edu/catalog/12045.html

von Rosenvinge, T. T., et al. 1995, Space Sci. Rev., 71, 155

Wang, Y.-M., 2012, Space Sci. Rev, 172, 123, DOI 10.1007/s11214-010-9733-0

Wang, Y.-M., & Sheeley, N. R. 1992, ApJ, 392, 310

Wang, Y.-M., & Sheeley, N. R. 2006, ApJ, 653, 708

Wang, Y.-M., Pick, M., & Mason, G. M. 2006, ApJ, 639, 495

Wang, L., Lin, R.P., Krucker, S., & Mason, G.M. 2012, ApJ, 759, 69

Wiedenbeck, M.E. et al. 2010, ApJ, 719, 1212

Yashiro, S. et al. 2004, ASP Conf. Series, 325, 401

Zank, G. P., Rice, W. K. M., & Wu, C. C. 2000, J. Geophys. Res., 105, 25079

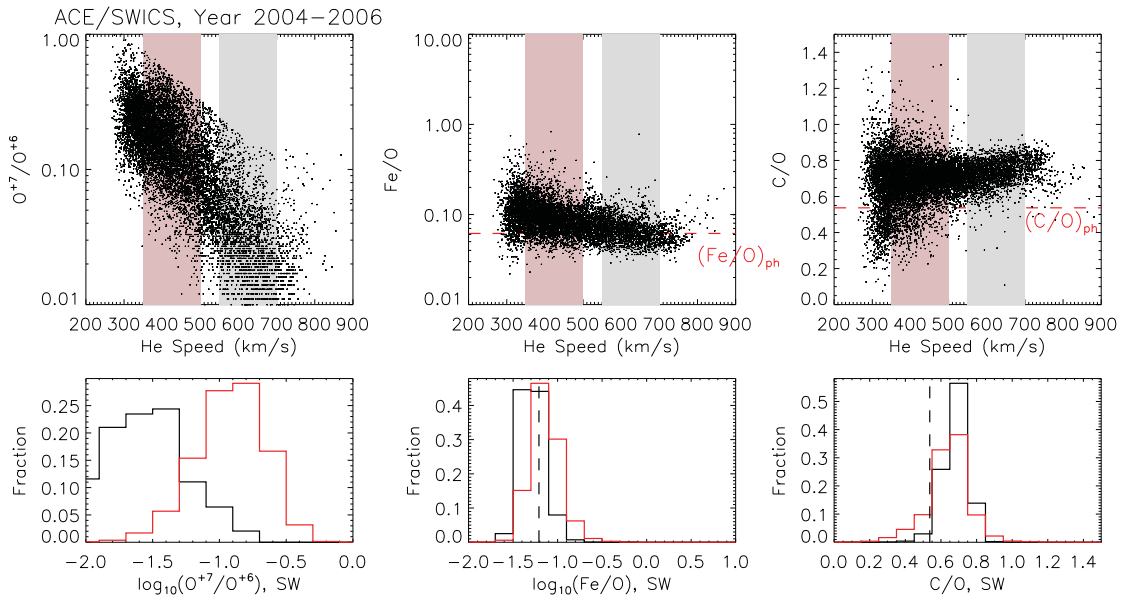Zank, G. P. et al. 2006, J. Geophys. Res., 111, DOI:10.1029/2005JA011524

Fig. 1.— Upper panels: O^{+7}/O^{+6} and abundance ratios Fe/O, C/O plotted against helium speed in non-ICME solar wind during years 2004-2006 measured by ACE/SWICS (2-hr average, Level-2 data). Lower panels: Comparison of histogram distribution for typical slow SW (350-500 km/s, range marked by light red in the upper panels) and fast SW (550-700 km/s, range marked by grey in the upper panels). The y-axis is the fraction of occurrence in its individual class. The photospheric value (Asplund et al. 2009) for Fe/O and C/O is marked by the dashed line. A significant fraction of the slow SW and fast SW has similar range of Fe/O and C/O ratios. This reflects a large range of variations in their source region properties.
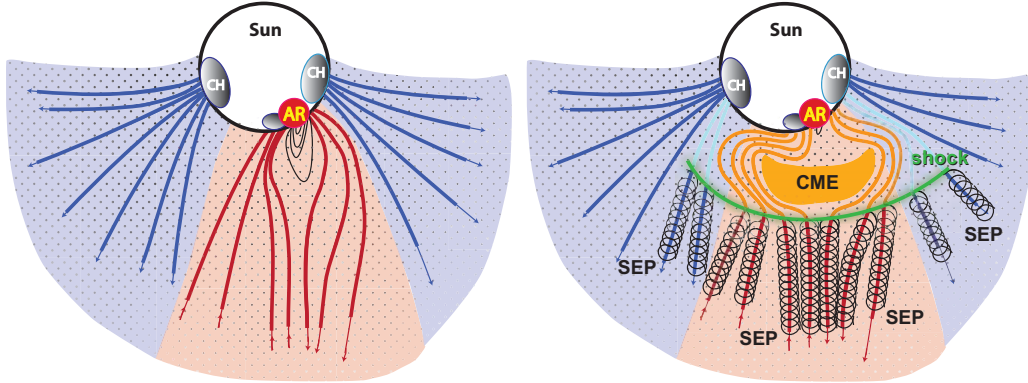
Fig. 2.— Left: IMF configuration and distribution of seed particles before the CME. Suprathermal seed particles populating these flux tubes have different properties according to their footpoint connection (blue or red patches). Right: Field line configuration and SEP production during the CME event. After the CME eruption, the CME shock accelerates upstream seed particles in these flux tubes to high energies. Note that these seed particles upstream of the CME shock are the same ones that populate the flux tubes *before* the eruption, even if the shock interception, distorted field and/or reconnection changed the particle properties in the downstream region. Therefore, the measured SEPs before the ICME arrives in-situ still reflect the composition of seed particles that were present before the CME occurred and hence are characteristic of the original IMF-footpoint region.
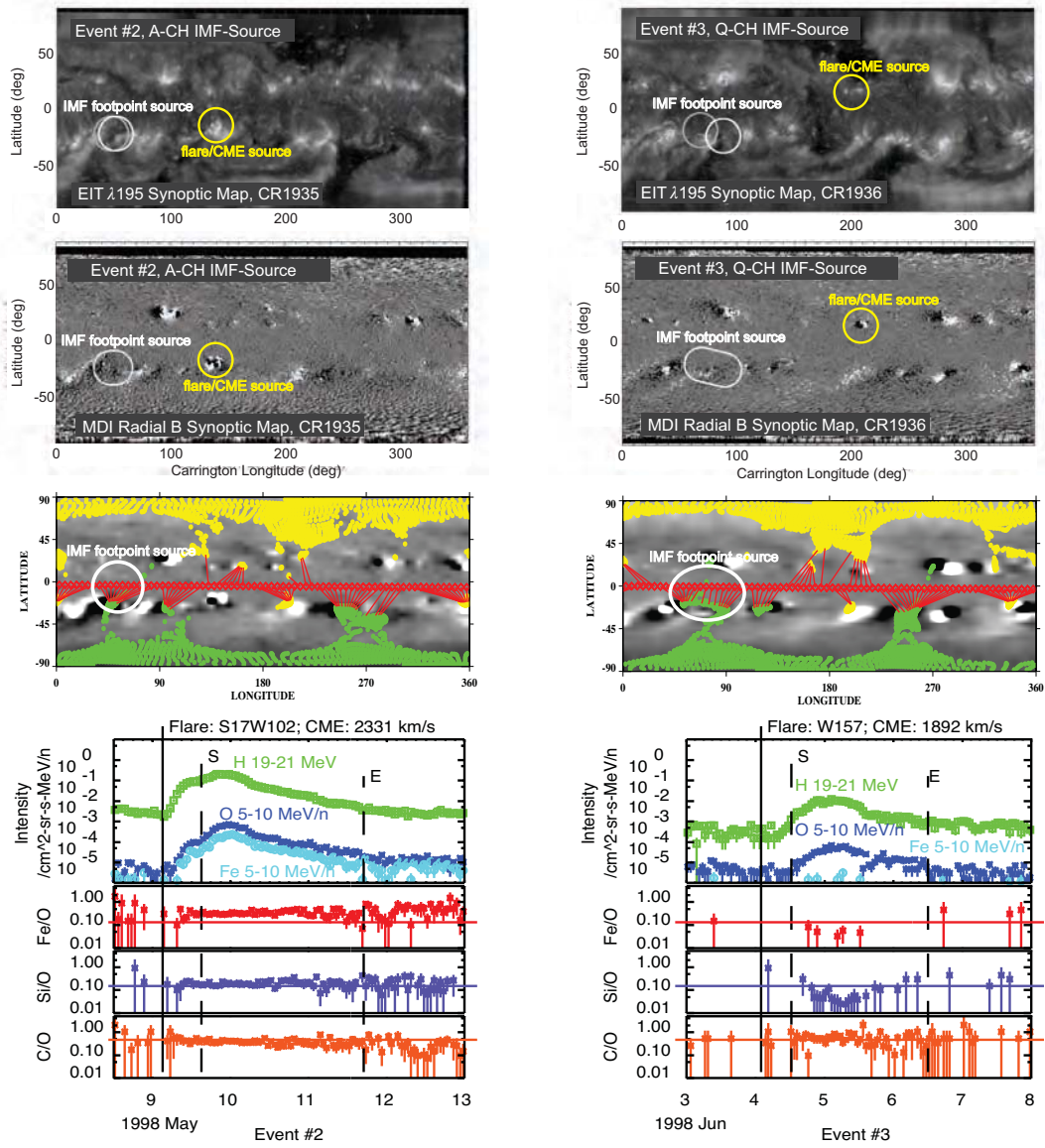
Fig. 3.— Data overview for two events, #2 (left column) and #3 (right column). In each column, the panels from top to bottom are: the synoptic Carrington map from SOHO/EIT; the synoptic Carrington map from SOHO/MDI; the synoptic map of the radial photospheric magnetic field (from NSO Kitt Peak for Event#2 and from MWO for Event #3), with results from the PFSS calculation overlaid; and time histories of hourly-averaged SEP intensities and elemental abundance ratios from Wind/EPACT. See text for further details.
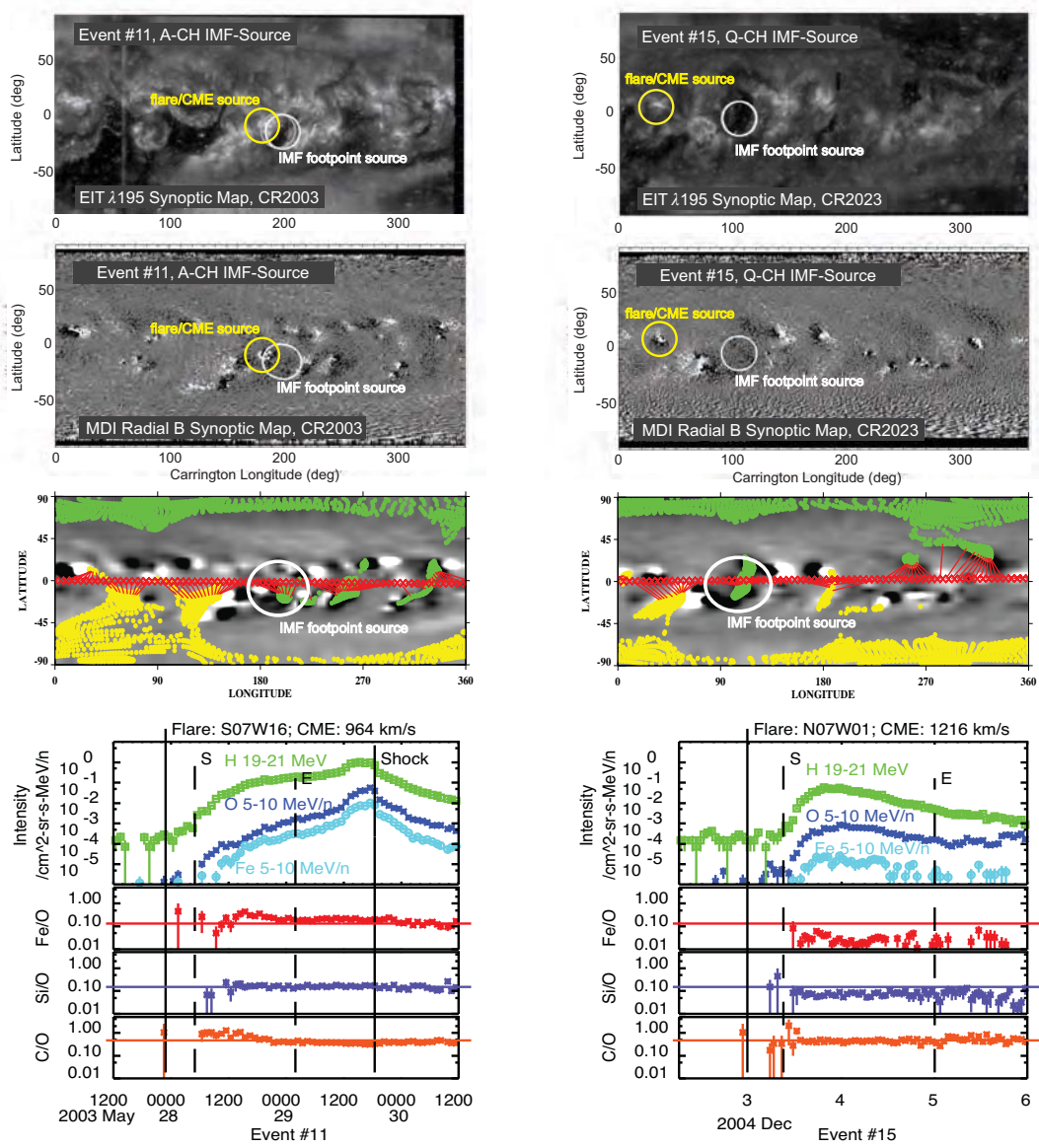
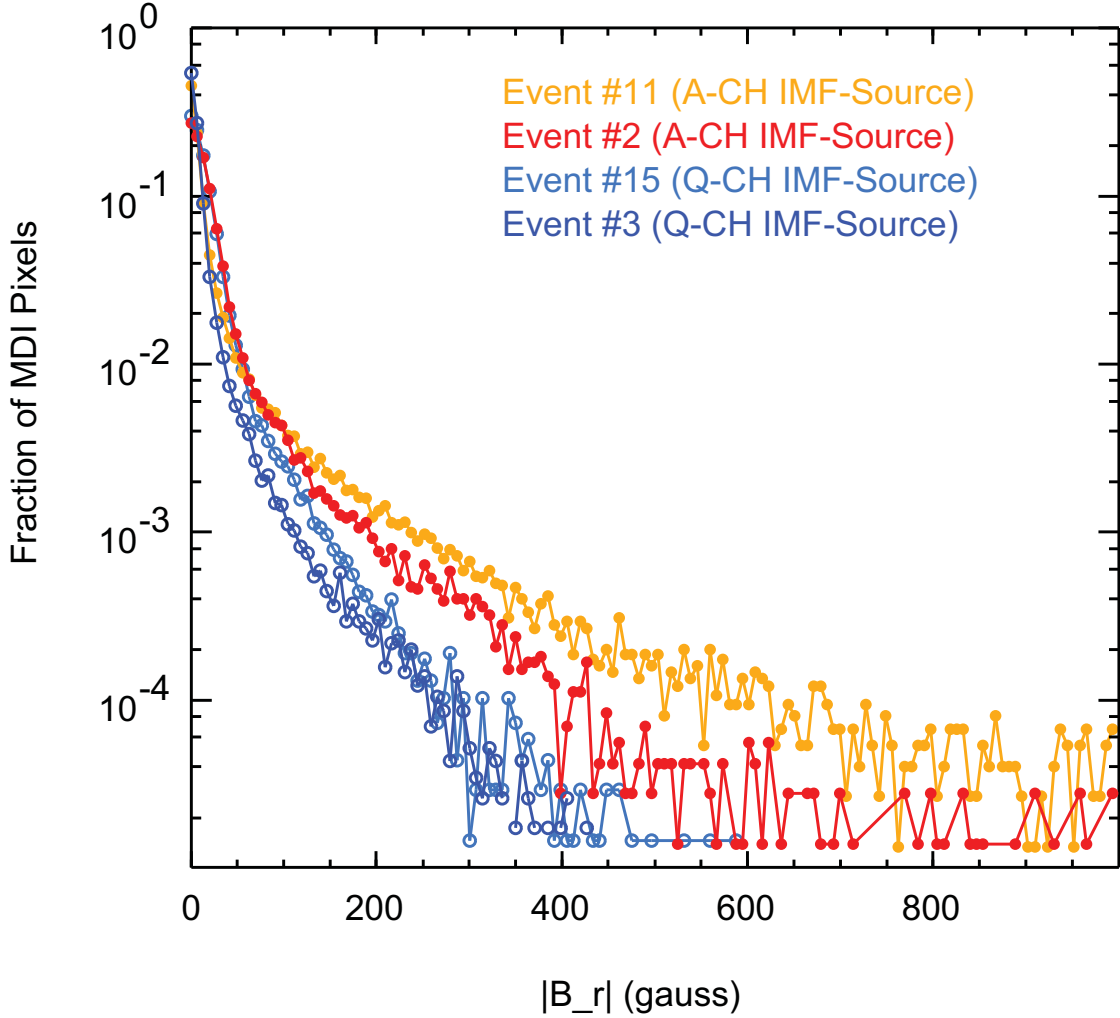Fig. 4.— Same as Fig. 3 but for Events #11 and #15

Fig. 5.— Histogram of the magnitudes of the radial component of the magnetic field strength in SOHO/MDI pixels within the IMF-footpoint regions of the events shown in Figures 3 and 4. These histograms are drawn from observations near the start time of the SEP event.
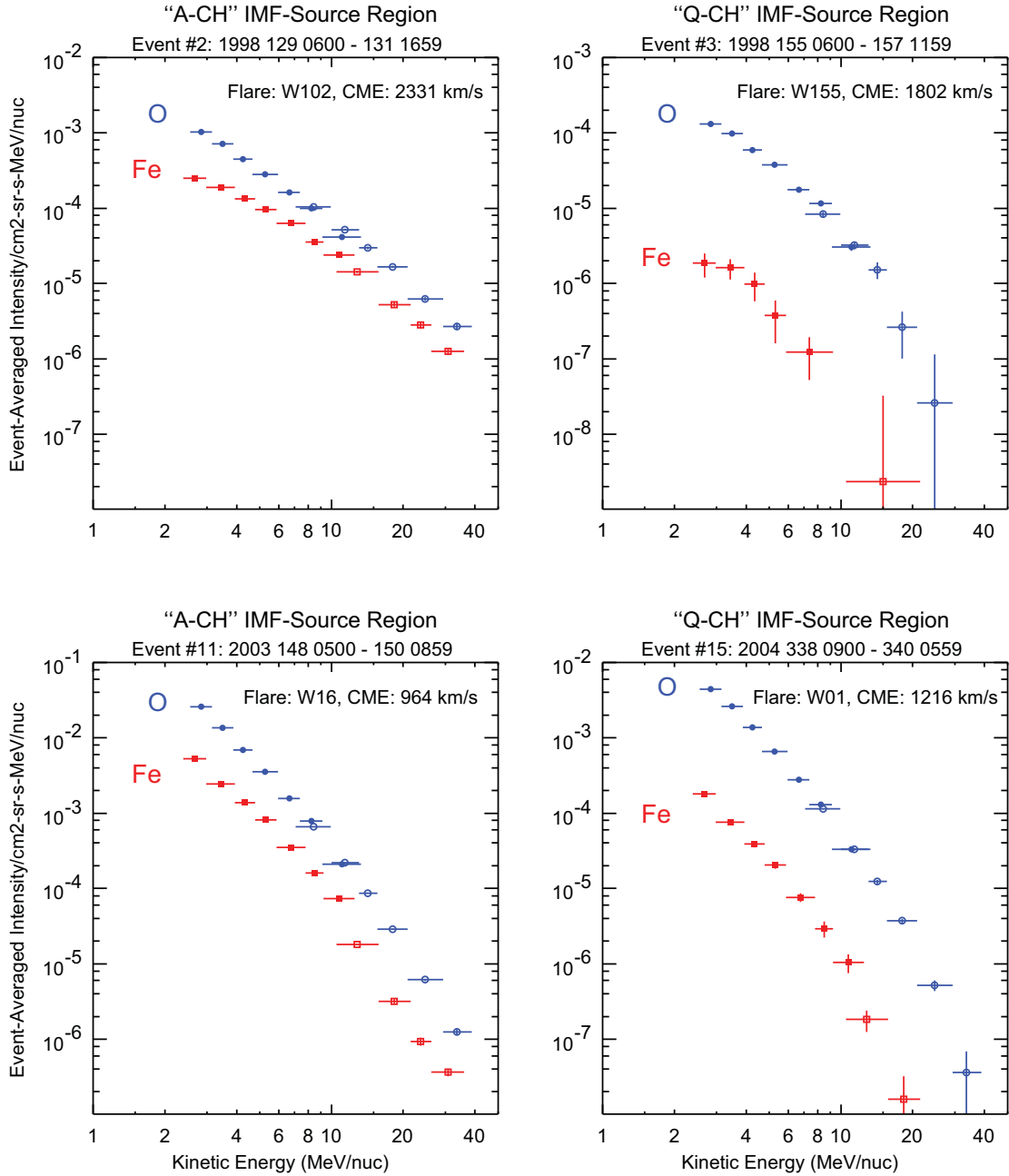
Fig. 6.— Event-averaged oxygen (blue) and iron (red) energy spectra for events with AR IMF-source regions (left column) and CH IMF-source regions (right column) for the events in Figure 3 (top panels) and Figure 4 (bottom panels). The number of decades on the axes are the same in all four panels so as to facilitate comparisons of spectral shapes. However, the dynamical range of intensities differ. Filled (open) symbols represent datapoints from Wind/LEMT (ACE/SIS). In each event, a small global adjustment factor has been applied to the ACE/SIS measurements so as to minimize normalization discrepancies between the instruments.
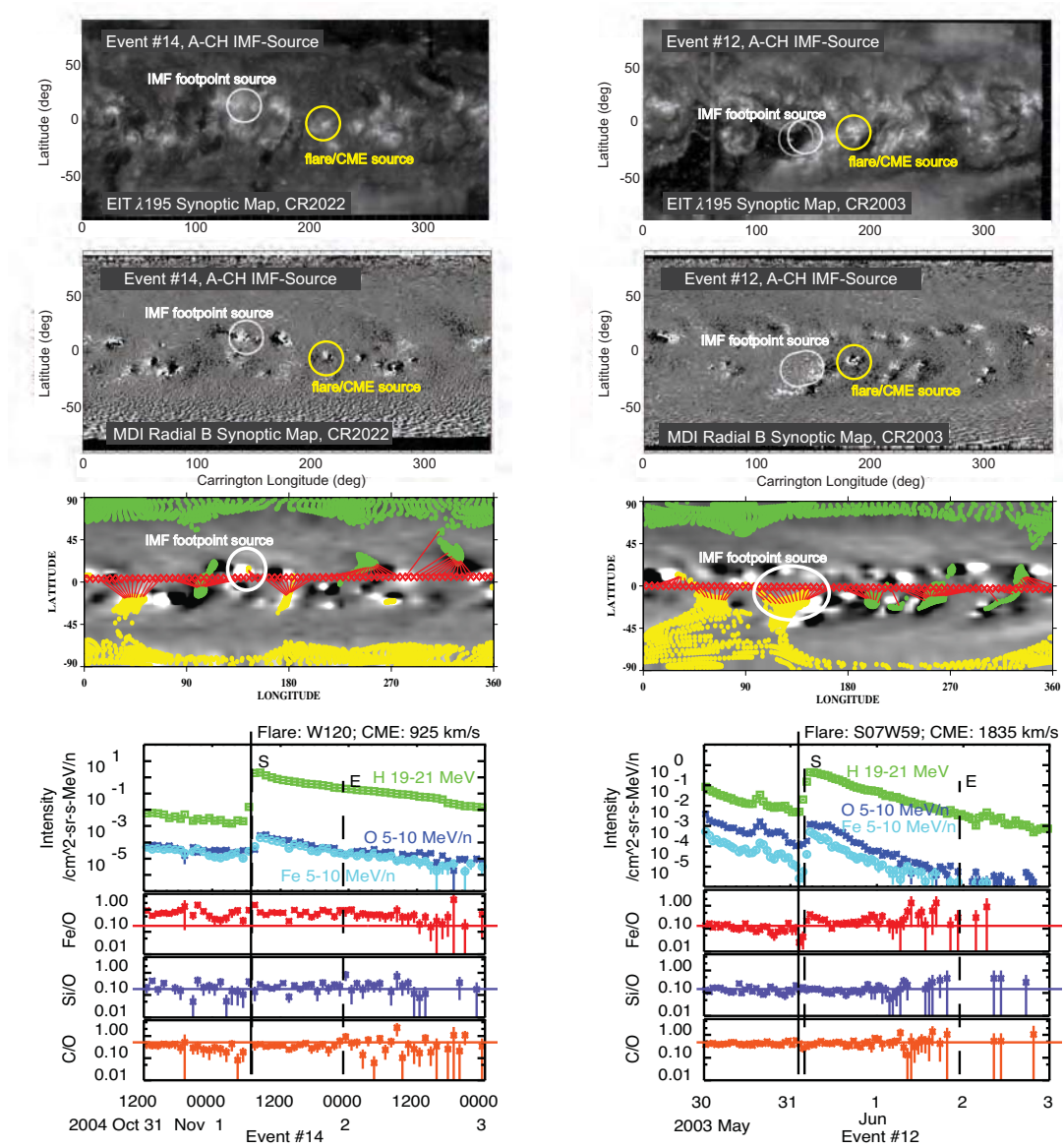
Fig. 7.— Same as Fig. 3 but for two more events with A-CH IMF-source regions, #14 (left) and #12 (right).
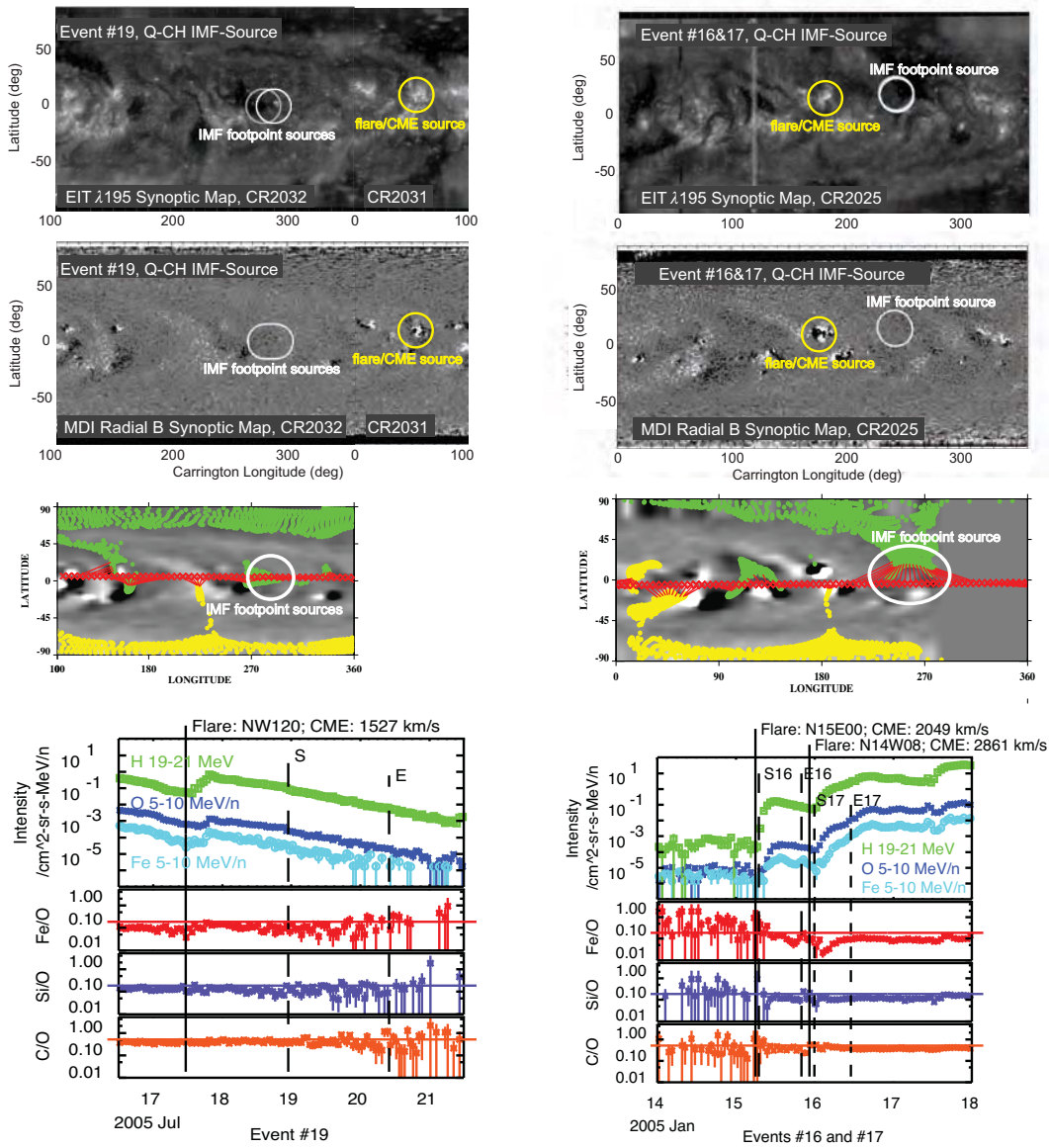
Fig. 8.— Same as Fig. 3 but for more events with Q-CH IMF-source regions, #19 (left) and # 16 and #17 (right). In the left column, the EIT and MDI maps are stitched together from two successive Carrington maps so that the flare/CME source and the IMF-source can both be shown. In the right column, the Mt. Wilson photopsheric field has a datagap for Carrington longitudes ∼280-360 degrees. However, PFSS calculations with field maps from NSO Kitt Peak and Wilcox observatory, which had no datagaps, gave essentially the same results for the IMF footpoint location.

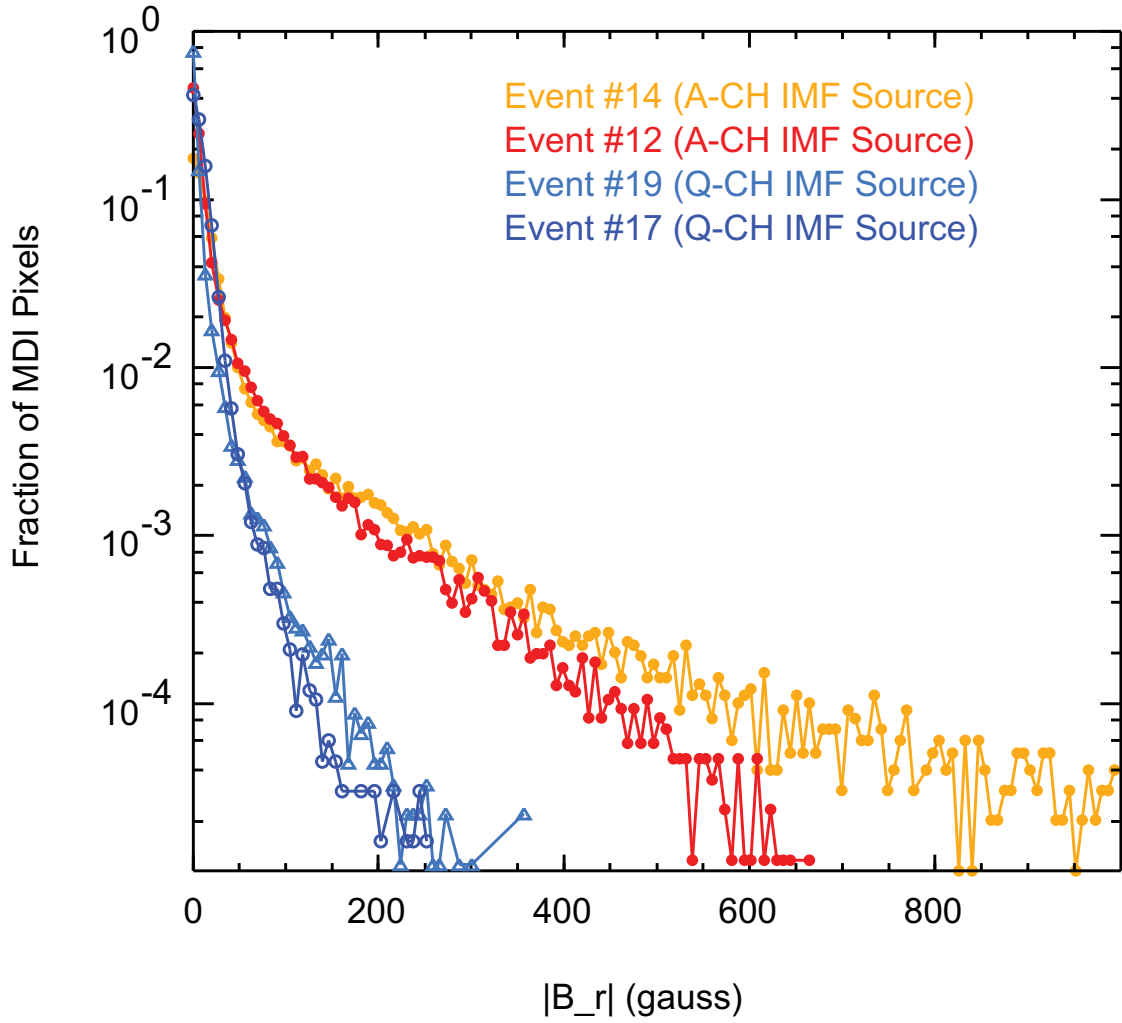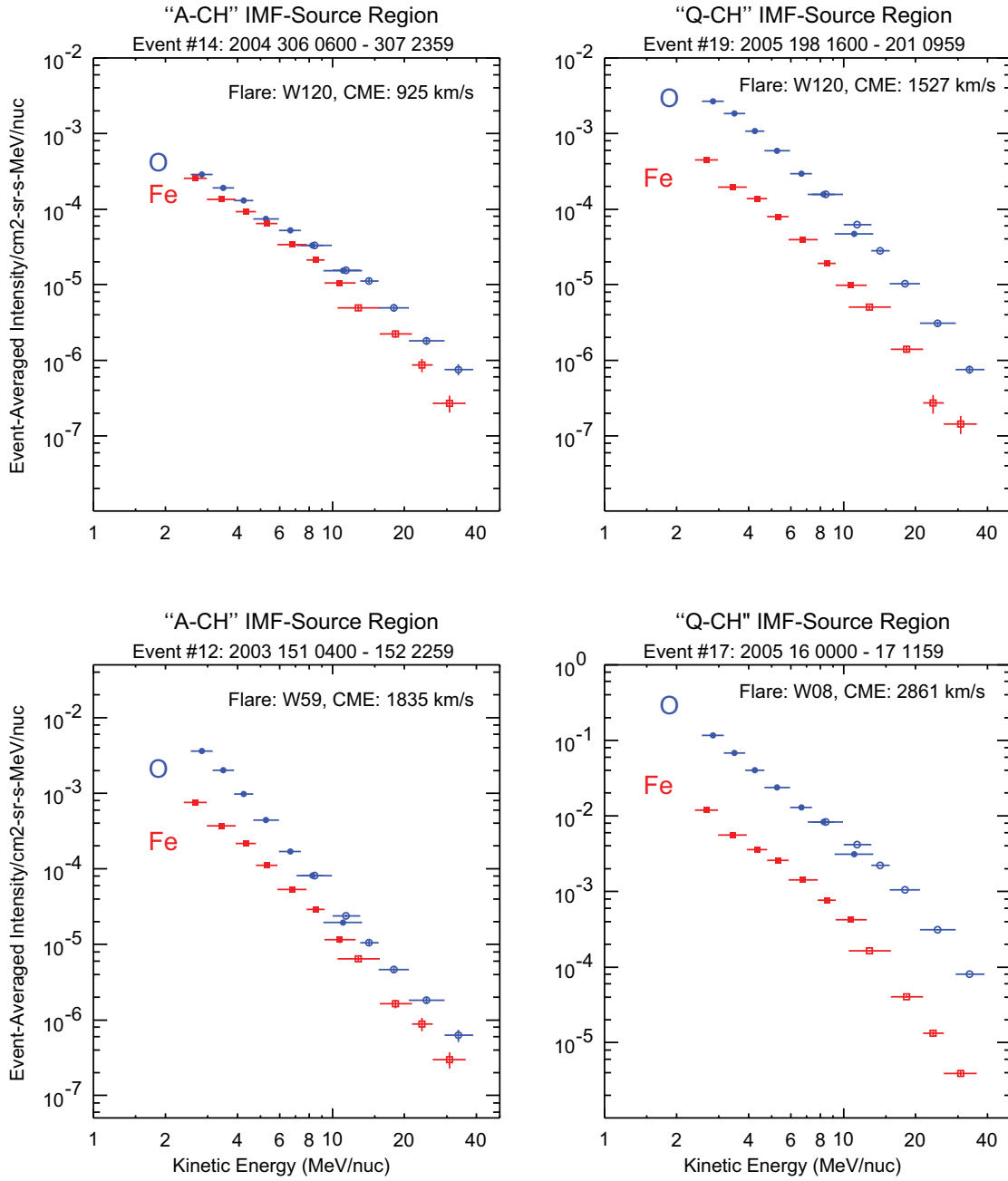Fig. 9.— Same as Fig. 5, but for the four events in Figures 7 and 8.

Fig. 10.— Same as Fig. 6, but for the four events in Figures 7 and 8.
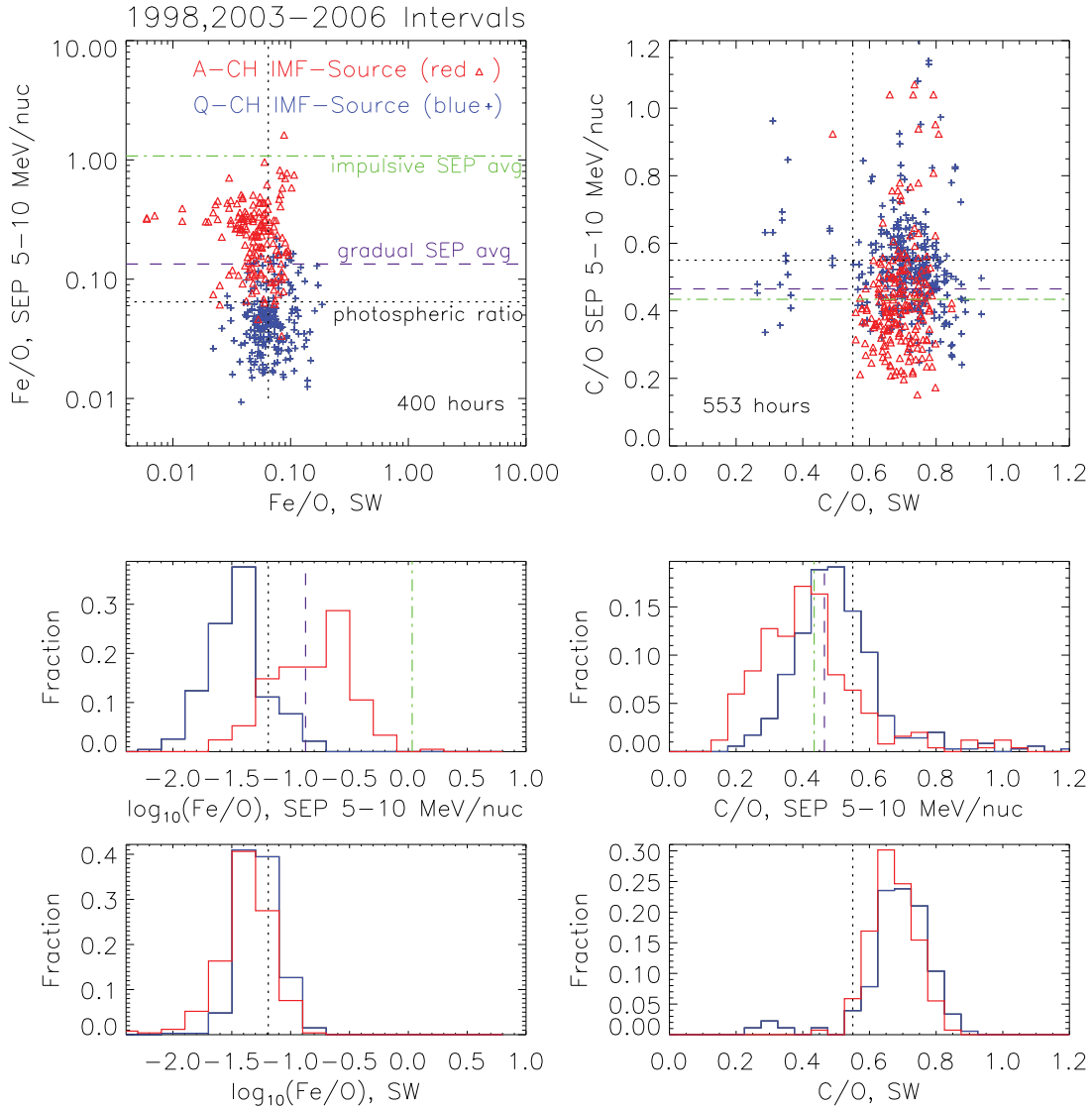
Fig. 11.— SEP Fe/O (left) and C/O (right) from WIND/EPACT/LEMT (5-10 MeV/nucleon, hourly data) vs those in the upstream *thermal* SW from ACE/SWICS (level-2 data, hourly data for Fe/O, 2-hr data for C/O expanded to hourly bins assuming C/O is constant over 2 hours) for 25 SEP intervals. Number of hourly-measurements are noted on each correlation plot, with roughly two-thirds coming from Q-CH IMF-sources. Only SW measurements with quality flag equal to 0 or 1 are used in this analysis (see SWICS online data release notes). Error bars are unavailable for the SW ratios. On the SEP ratios, error bars (85% of which are less than 50%) are suppressed for clarity. Also plotted are histograms for the two types of IMF-sources in SEPs (middle panels) and SW (lower panels). Lines mark the average Fe/O and C/O values (Reames 1995) for impulsive SEPs (green dash-dot) and gradual SEPs (purple dashed) and for the photospheric value (black dotted, Asplund et al. 2009).
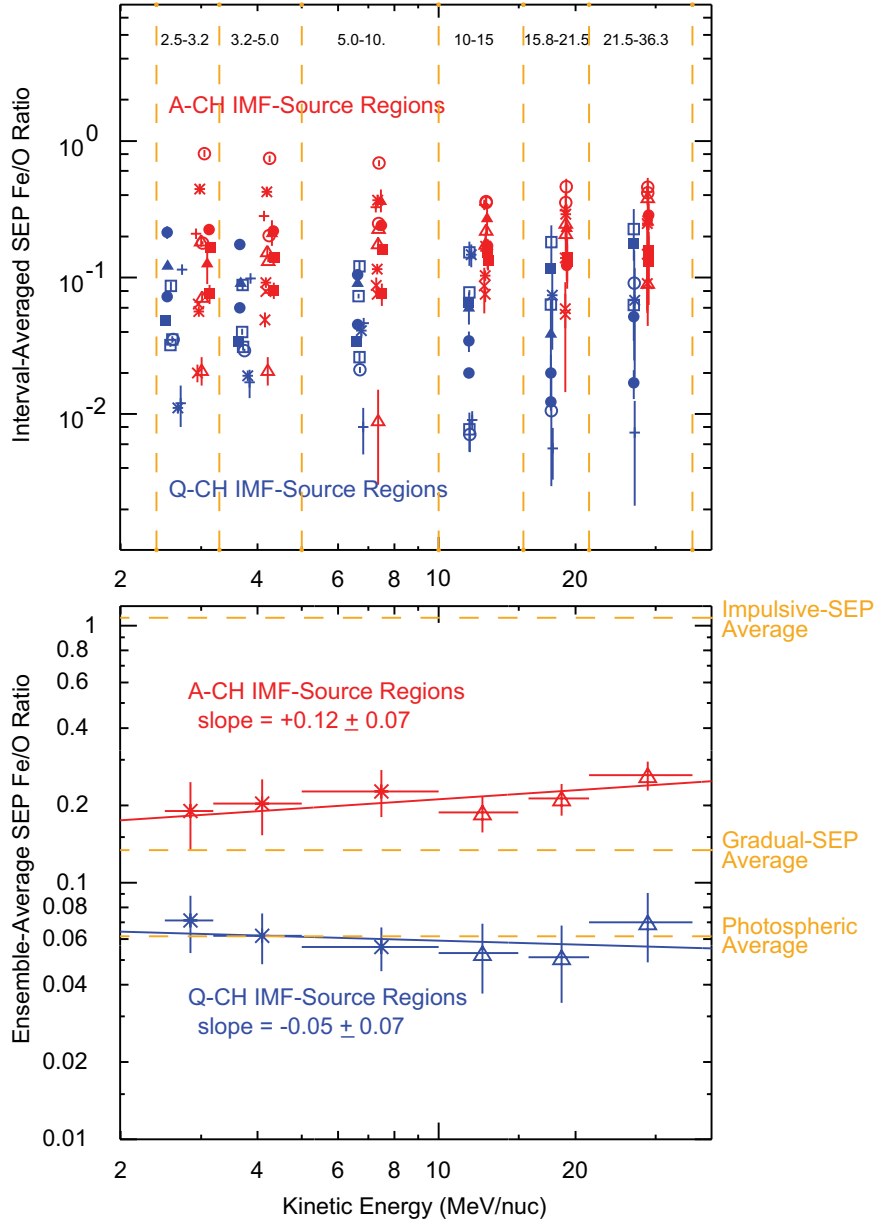
Fig. 12.— Top: Measured Fe/O values in different energy intervals (demarcated by vertical dashed lines and noted along the top of the plot) for the time-intervals in this study, with A-CH IMF-sources in red and Q-CH IMF-sources in blue. Measurements in the lower (upper) three energy intervals come from Wind/EPACT/LEMT (ACE/SIS). Bottom: Ensemble-average of the Fe/O ratios versus energy, shown separately for the A-CH and Q-CH IMF-sources in red and blue, respectively. A power-law fit is shown for each case, with the fitted value of the slope noted. For comparison, the dashed horizontal lines mark the impulsive and gradual-SEP Fe/O averages at 5-12 MeV/nucleon from Reames (1995) and the photospheric Fe/O value from Asplund et al. (2009).
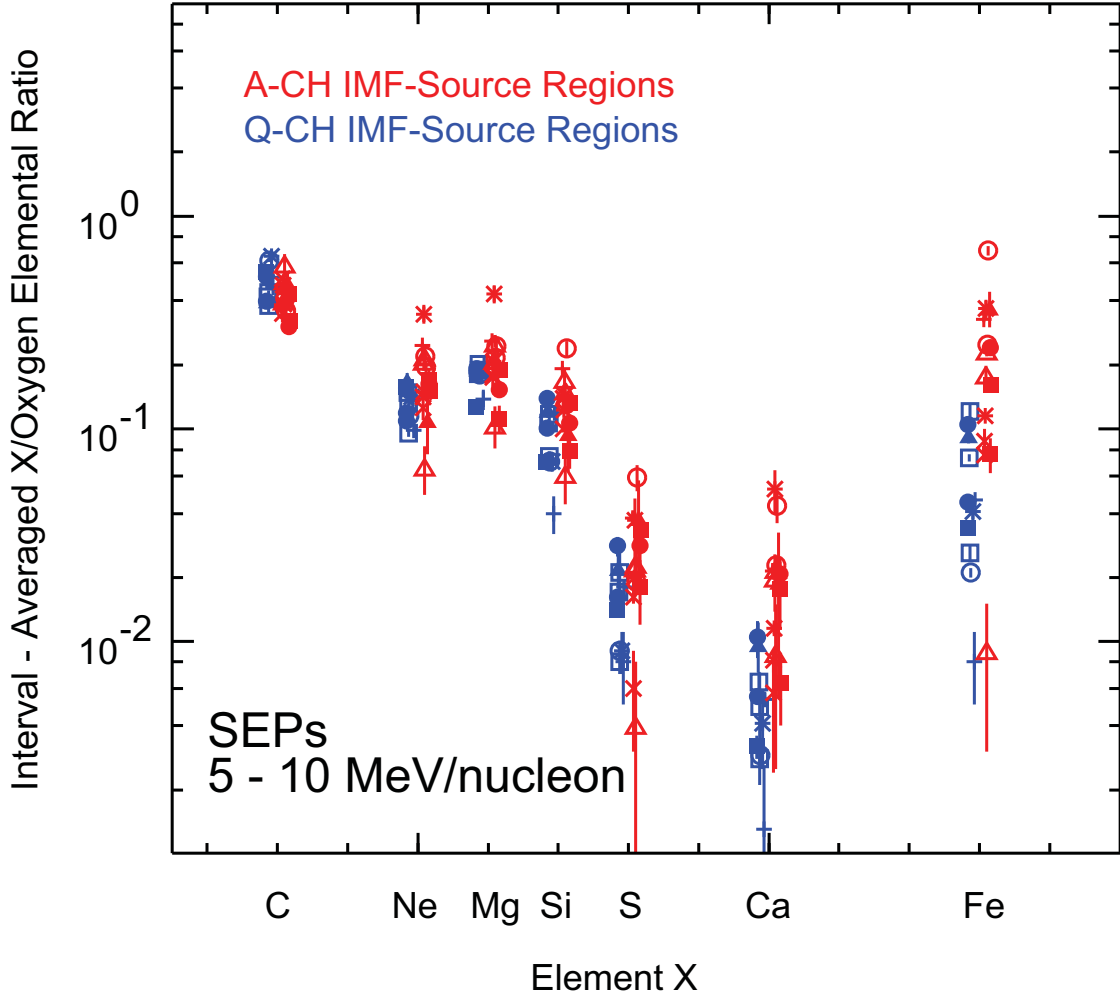
Fig. 13.— Interval-integrated elemental ratios relative to oxygen at 5-10 MeV/nucleon from Wind/EPACT/LEMT plotted versus atomic number, with symbols distinguishing among intervals. The abscissae have been slightly displaced in order to separate the datapoints visually. The symbols are color-coded according to the identified type of IMF-source, with red for A-CH and blue for Q-CH.
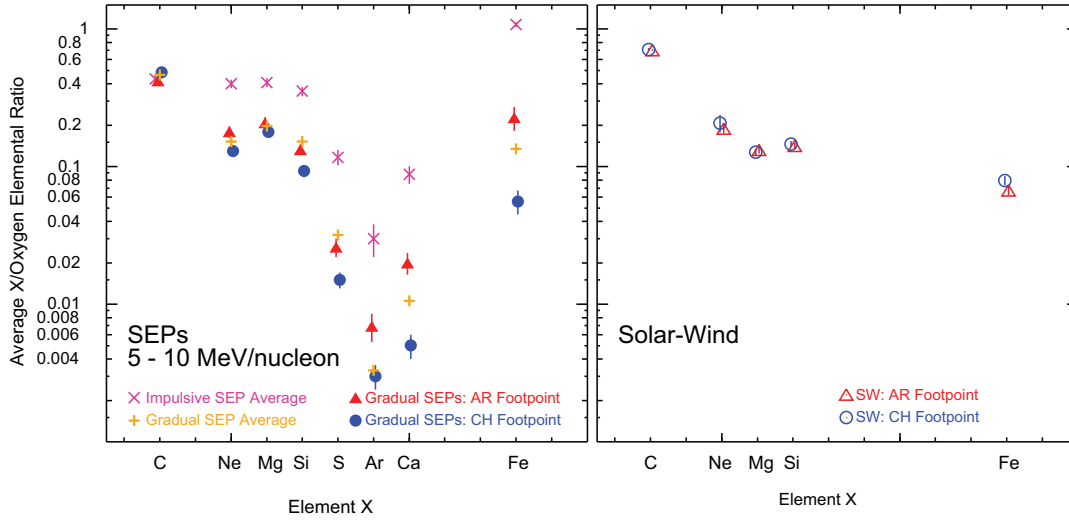
Fig. 14.— Left: Ensemble-averaged elemental ratios relative to oxygen at 5-10 MeV/nucleon from Wind/EPACT/LEMT for A-CH IMF-source regions (red filled triangles) and Q-CH IMF-source regions (blue filled circles). Also shown for comparison are average values for impulsive (pink asterisks) and gradual events (gold crosses) at 5-12 MeV/nucleon from Reames 1995. Right: Ensemble-averaged solar-wind elemental ratios from ACE/SWICS for time-intervals in this study, for A-CH IMF-source regions (red open triangles) and Q-CH IMF-source regions (blue open circles).
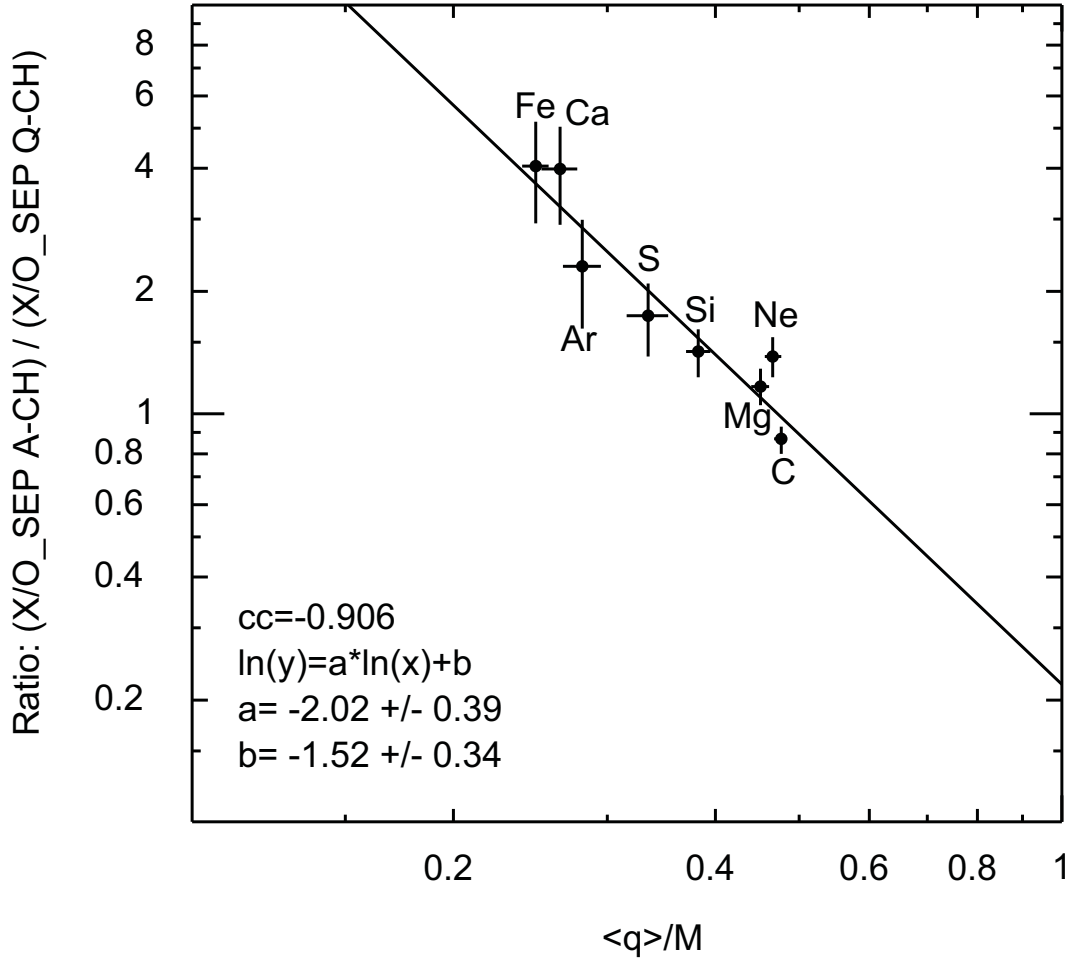
Fig. 15.— Ratio of ensemble-averaged elemental relative abundances (as specified by each element's ratio to oxygen) in A-CH IMF-source regions to that in Q-CH IMF-source regions. The ratio of abundances is plotted versus the nominal charge to mass ratio, $<q>/M$, where M is the mass number and $<q>$ is the average ionic charge measured in gradual SEP events (Luhn et al. 1984). Also shown is a power-law fit to the ratio.
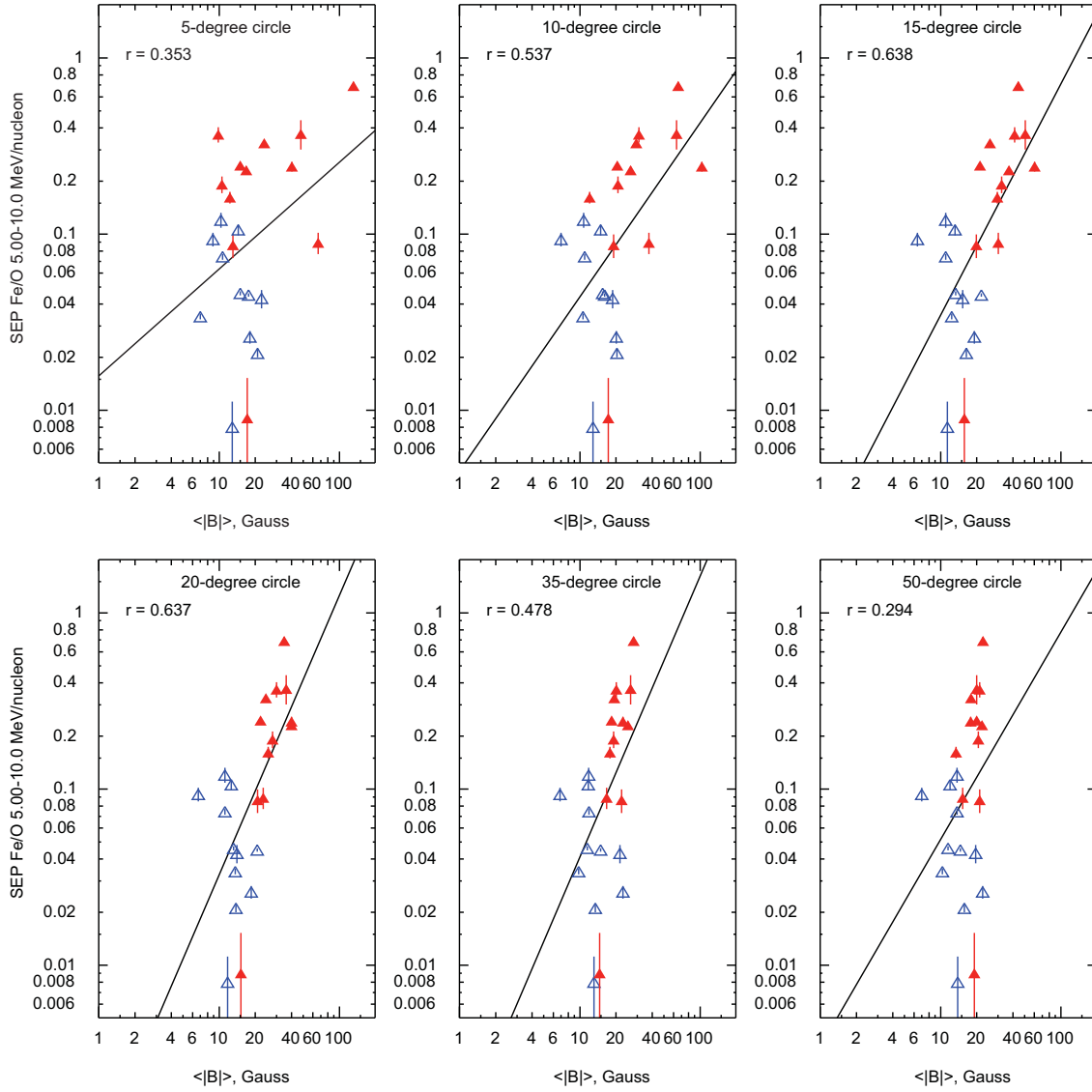
Fig. 16.— Scatter plots of the interval-integrated Fe/O at 5-10 MeV/nucleon versus the $< |B| >$ for six different radial sizes of the circular area around the footpoint over which B values were averaged. The radial sizes, noted at the top of each panel, range from 5° to 50°. Filled red triangles and open blue triangles stand for the A-CH and Q-CH IMF-source types, respectively Also shown are the correlation fits and the corresponding Pearson correlation coefficient.
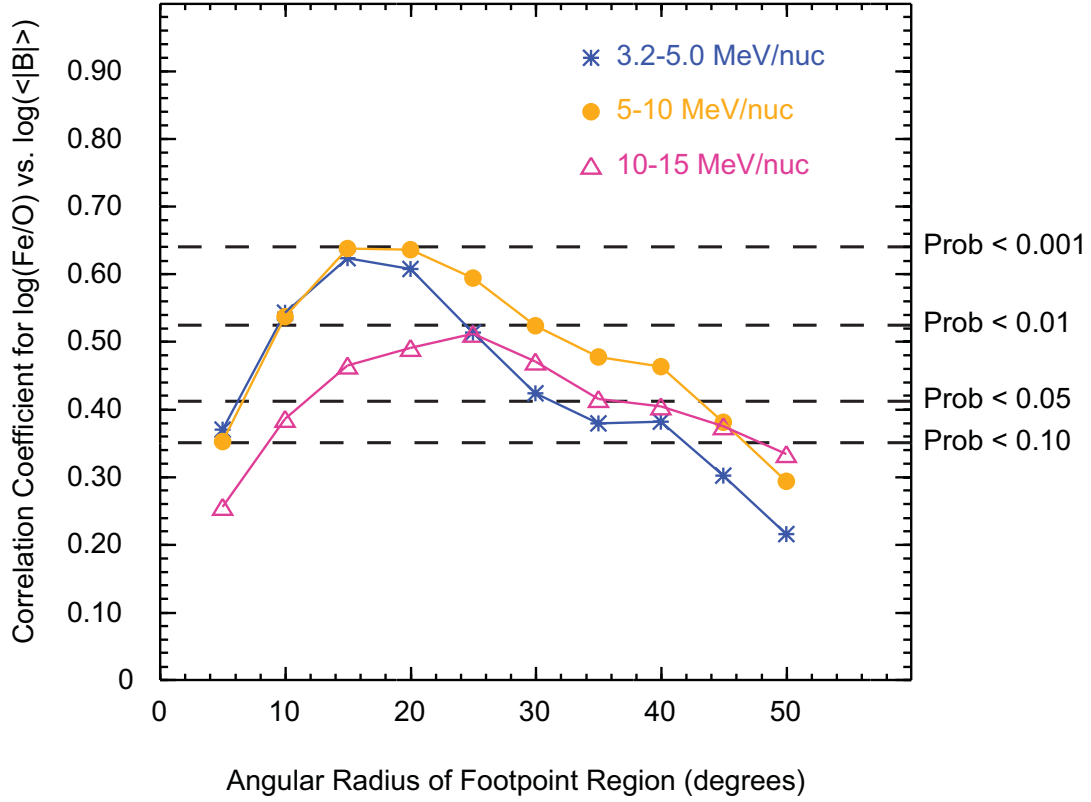
Fig. 17.— Pearson correlation coefficient versus the radial size of the footpoint region over which the magnetic field strength was averaged. The dashed horizontal lines show the values of the correlation coefficient corresponding to random probabilities of 0.10, 0.05, 0.01, and 0.001 (or, correspondingly, confidence levels of 90%, 95%, 99%, and 99.9%, respectively) for a sample size of 23. The results are shown for three different Fe/O energy intervals. Highly-significant correlations occur for averaging circles with radii of ∼15-30°.
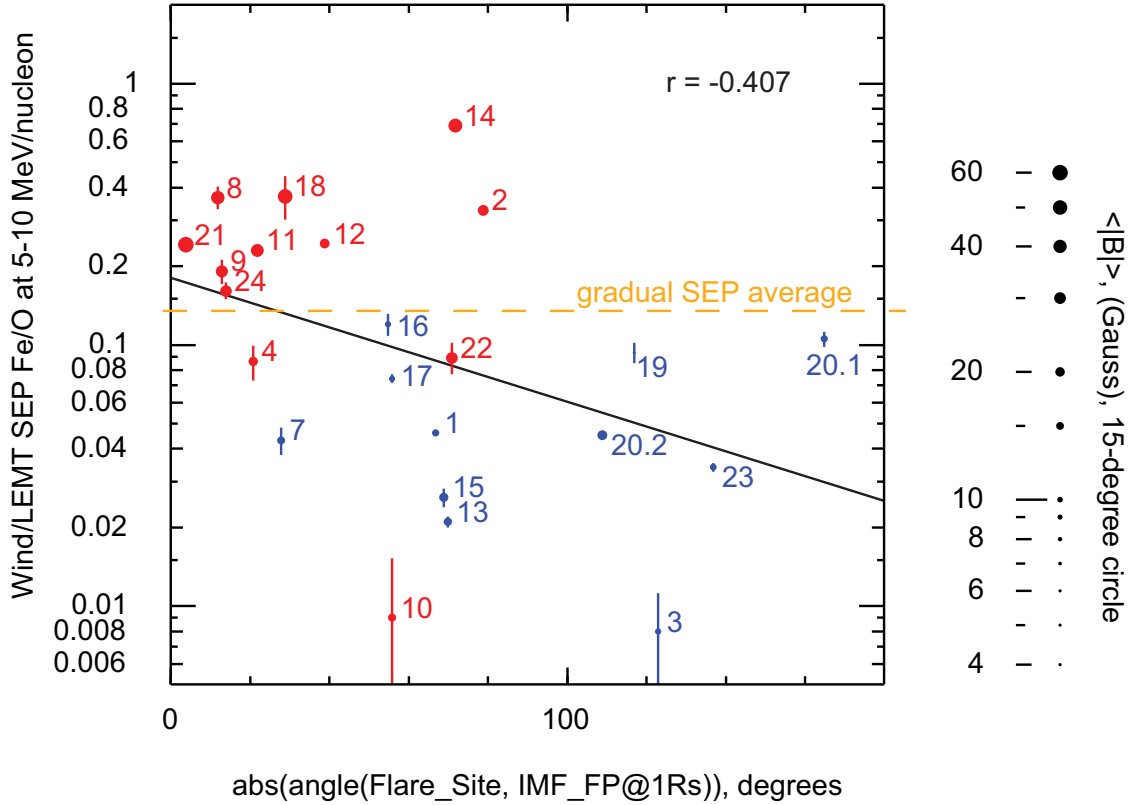
Fig. 18.— Interval-integrated Fe/O at 5-10 MeV/nucleon vs. the angular separation (in degrees) between the flare source and the IMF footpoint, evaluated at the Sun at 1 $R_{\odot}$. Events with Q-CH and A-CH IMF-source regions are blue and red, respectively. As explained in the legend at the right, the symbol size reflects the magnitude of the average magnetic field at the IMF-source region. Event numbers are marked on the plots. The correlation fit and its correlation coefficient are also shown on the plot. Events 5 and 6, for which magnetic field data were not available, are not shown but were included in the correlation fit. The dashed horizontal line marks the average Fe/O value for gradual SEP events at 5-12 MeV/nucleon (Reames 1995).
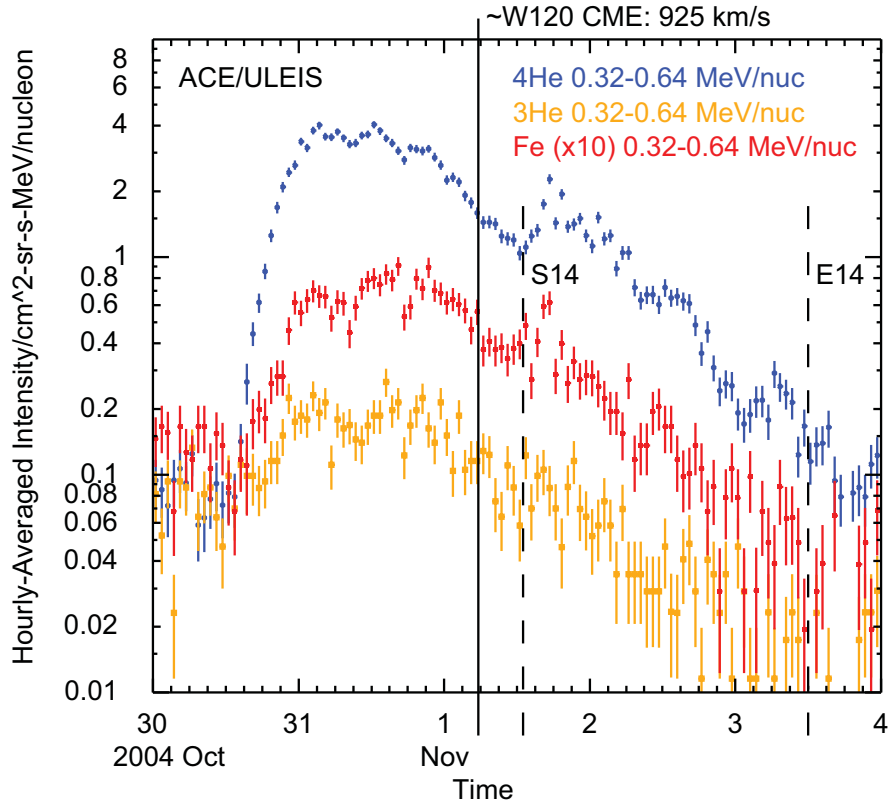
Fig. A1.— From Event #14: time profiles of hourly-averaged particle intensities for ^{4}He (blue), Fe (red, multiplied by 10), and ^{3}He (gold) at 0.32-0.64 MeV/nucleon from ACE/ULEIS. Dashed vertical lines mark the start- and end-times of the integration interval for these data. An increase associated with the marked CME is apparent in ^{4}He and Fe, but not in ^{3}He. As a result, only an upper limit can be reported on ^{3}He/^{4}He for this event.
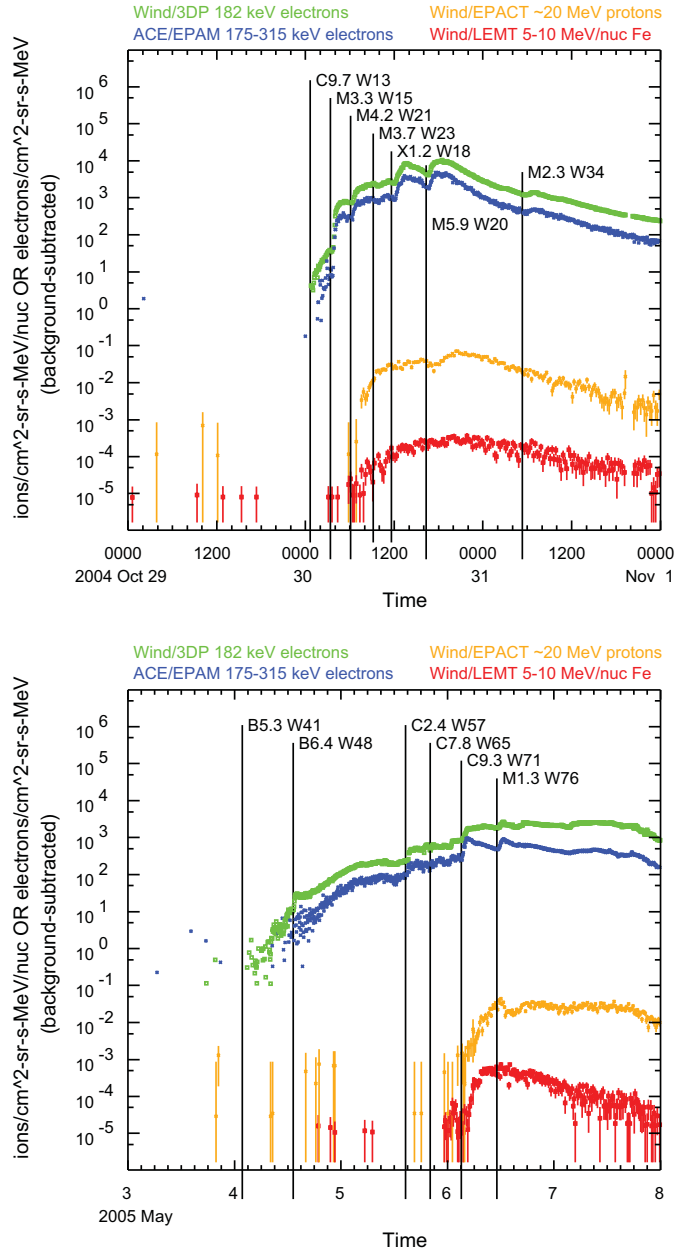
Fig. A2.— For Events I1 (top) and I2 (bottom): time-intensity profiles of near-relativistic electrons at ∼200 keV from Wind/3DP (green) and ACE/EPAM (blue), ∼20 MeV protons from Wind/EPACT (gold), and 5-10 MeV/nucleon iron ions from Wind/EPACT/LEMT (red). Pre-event background levels have been subtracted from the intensities. Electron data are five-minute averages; the proton and ion data are 15-minute averages. Vertical black lines mark the start times of the marked soft x-ray flares, as reported by GOES.
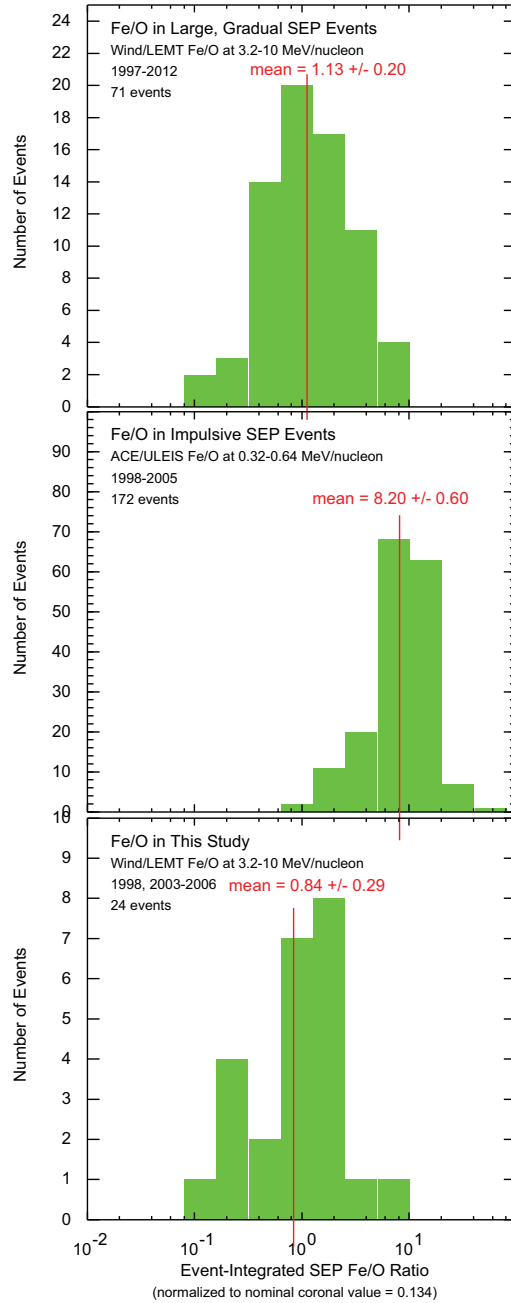
Fig. A3.— Histogram of event-integrated Fe/O values from large gradual events at 3.2-10 MeV/nucleon, as observed by Wind/EPACT/LEMT (top); from impulsive events at 0.32-0.64 MeV/nucleon from ACE/ULEIS (middle); and from the events selected in this study, also at 3.2-10 MeV/nucleon from Wind/EPACT/LEMT. Fe/O values are normalized to the nominal coronal value of 0.134 given by Reames (1995). Red vertical lines mark the calculated means of the distributions.
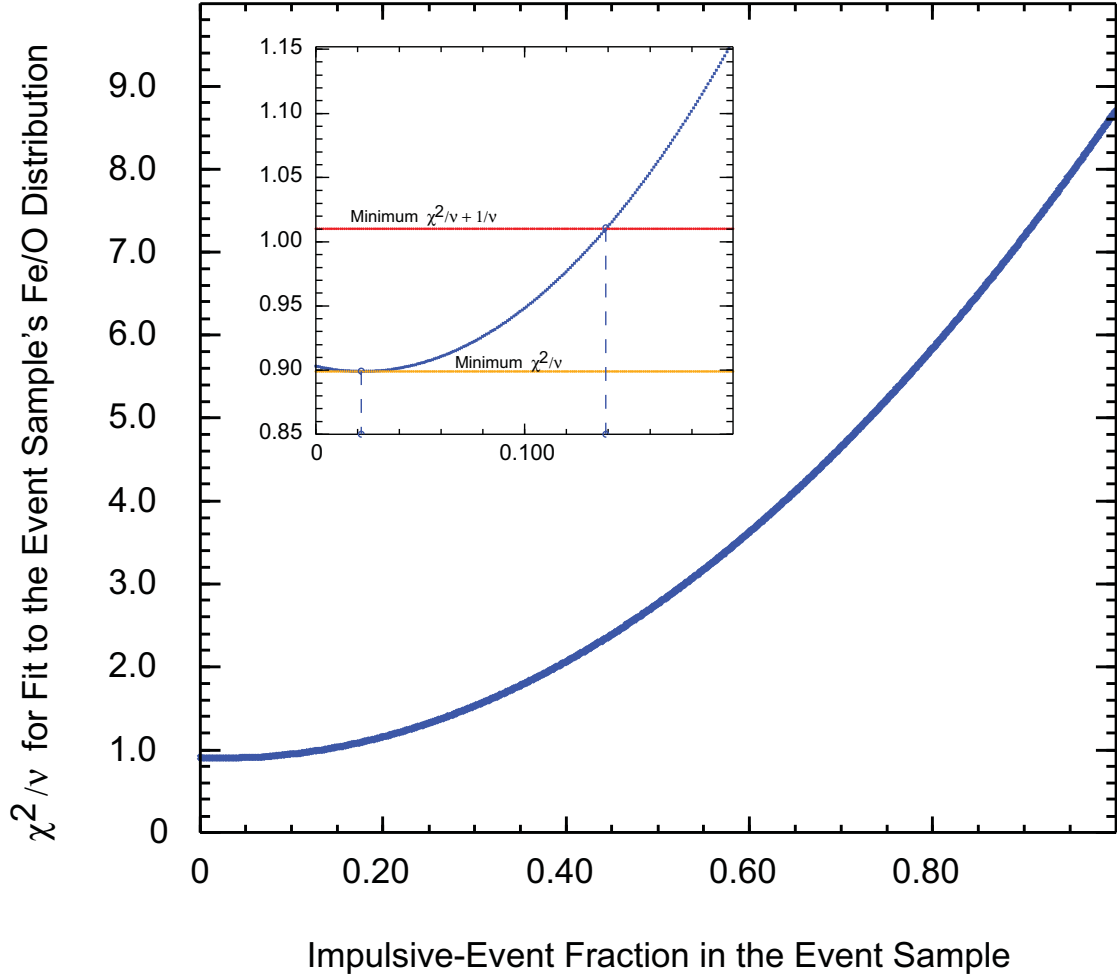
Fig. A4.— Calculated value of reduced χ^2 (from equation 2) versus impulsive-event fraction for the distribution of event-integrated Fe/O values (bottom panel, Figure A3) for the events in this study. The inset shows a closer view of the region near the minimum in χ^2/ν.
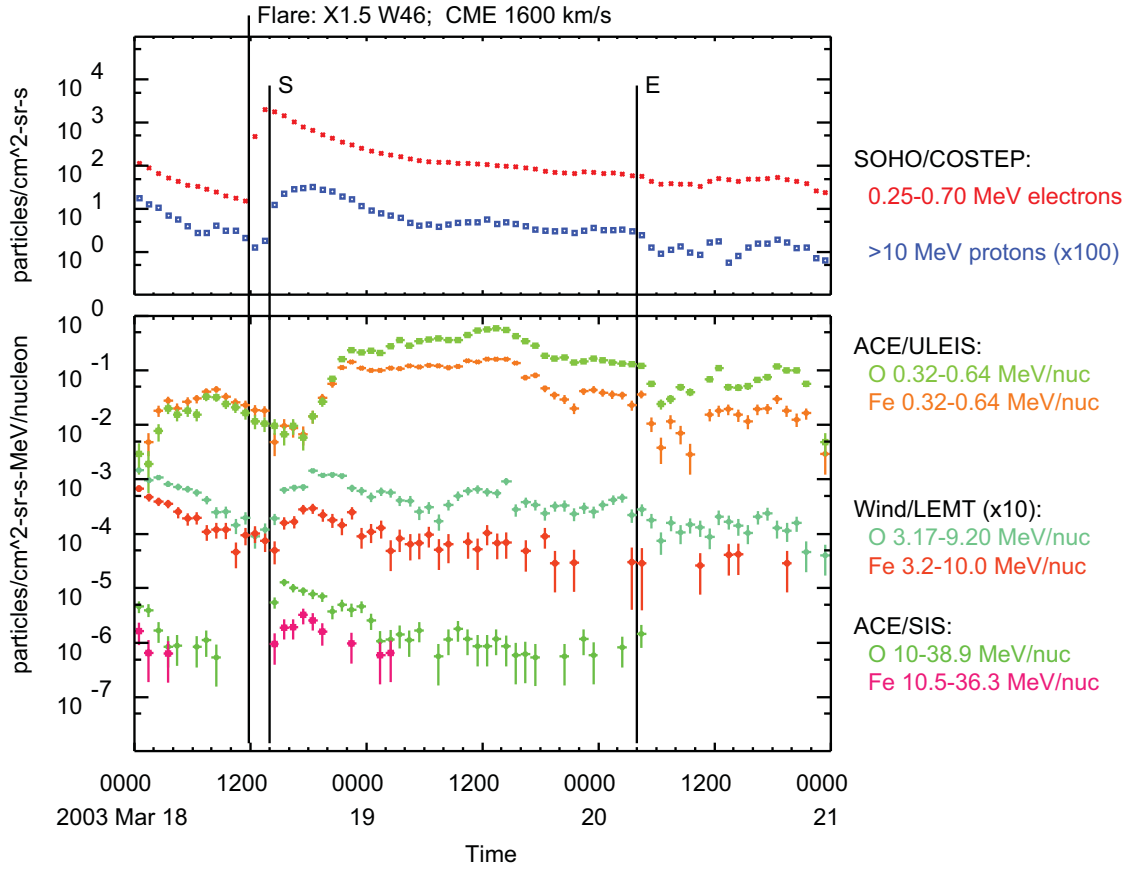
Fig. A5.— For Event #9: time profiles of hourly-averaged particle intensities for 0.25-0.70 MeV electrons and >10 MeV protons (from SOHO/COSTEP; top panel) and for O and Fe ions (bottom panel) at 0.32-0.64 MeV/nucleon (from ACE/ULEIS), 3.2-10.0 MeV/nucleon (from Wind/EPACT/LEMT), and ~10-35 MeV/nucleon (from ACE/SIS). Note that electron and proton intensities are integral in energy, while the ion intensities are differential. Also note that the >10 MeV protons and Wind/LEMT ions have been multiplied factors of 100 and 10, respectively, for graphical clarity. The vertical lines mark the start of the associated soft x-ray flare and the start (S) and end (E) of the time-interval used for calculating event-averaged quantities from Wind/LEMT and ACE/SIS. The start of the integration interval was delayed by four hours for ACE/ULEIS quantities.
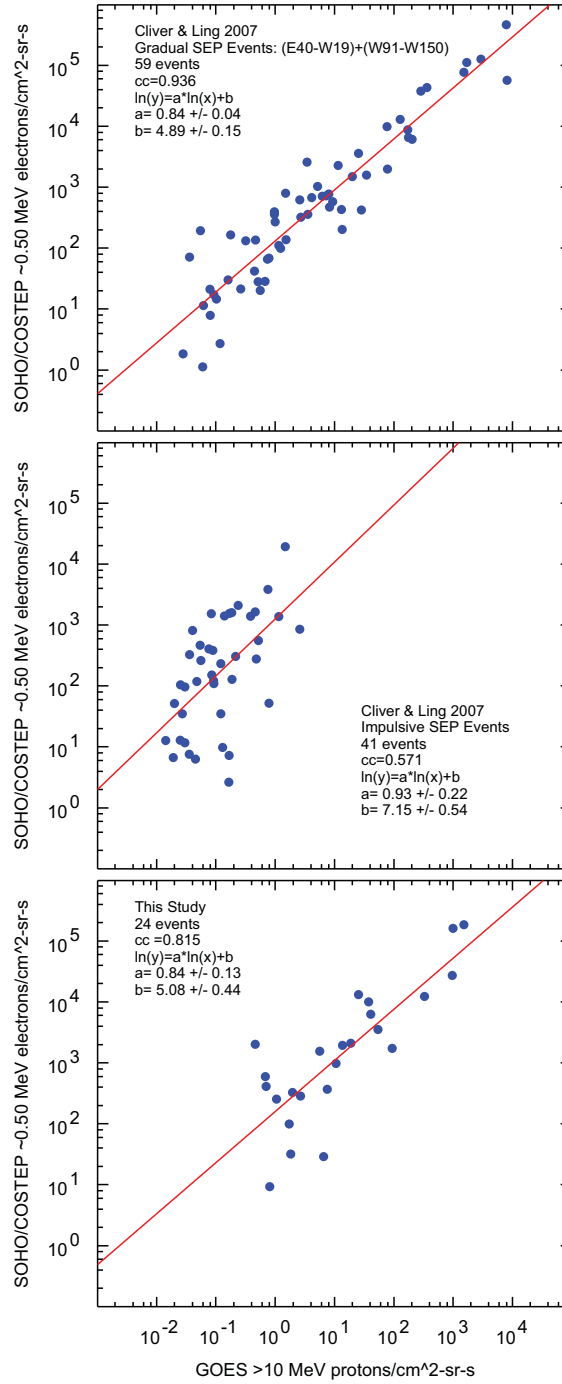
Fig. A6.— Correlation plot of the peak hourly-averaged intensity of electrons at 0.25-0.70 MeV from SOHO/COSTEP versus the peak hourly-averaged intensity of >10 MeV protons from GOES for gradual events (top) from Cliver & Ling (2007); impulsive events (middle) from Cliver & Ling (2007); and from events in this study (bottom.) Least-squares correlation fits are also shown, along with the correlation coefficients and the fitted parameters.
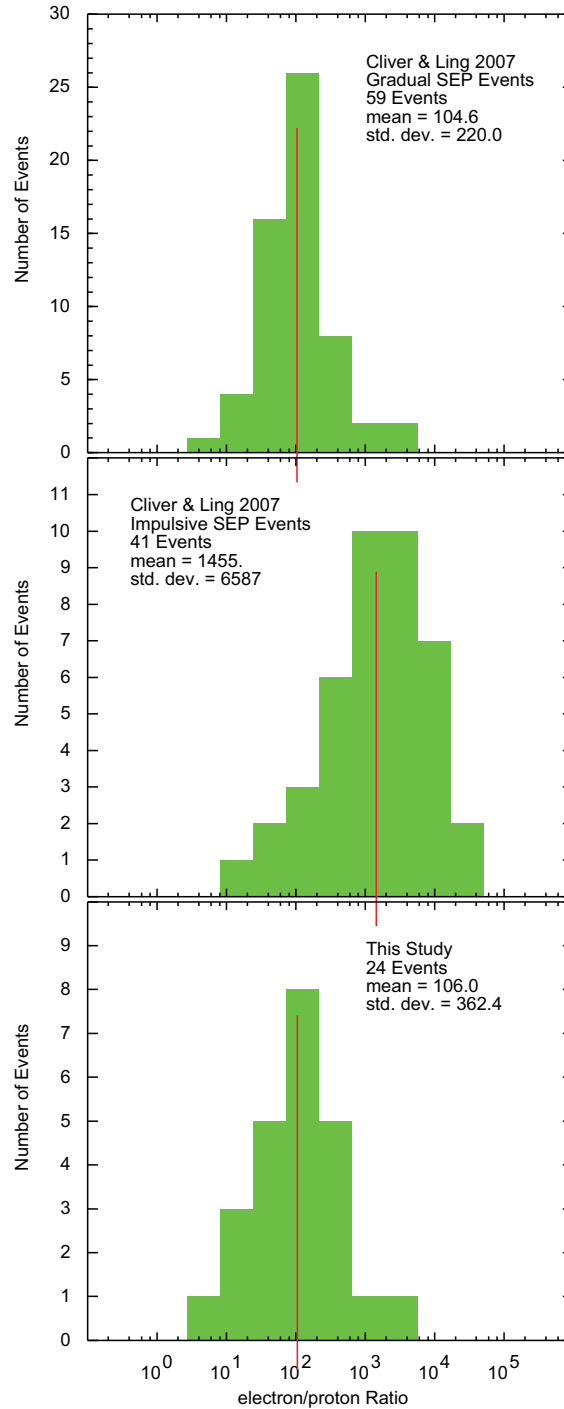
Fig. A7.— Histogram of e/p ratios for gradual SEP events (top) from Cliver & Ling (2007); for impulsive SEP events (middle) from Cliver & Ling (2007); and from the events selected in this study. Red vertical lines mark the calculated means of the distributions.

Fig. A8.— For Event #14: time profiles of 5-minute-averaged particle intensities from SOHO/COSTEP for 0.25-0.70 MeV electrons (blue) and 25-63 MeV protons (red, and multiplied by 1000). Vertical lines mark the start of the M1.1 flare that preceded Event #14 and the launch of the relevant CME.

Table 1.　1998,2003-2006 SEP Intervals Selected for Analysis

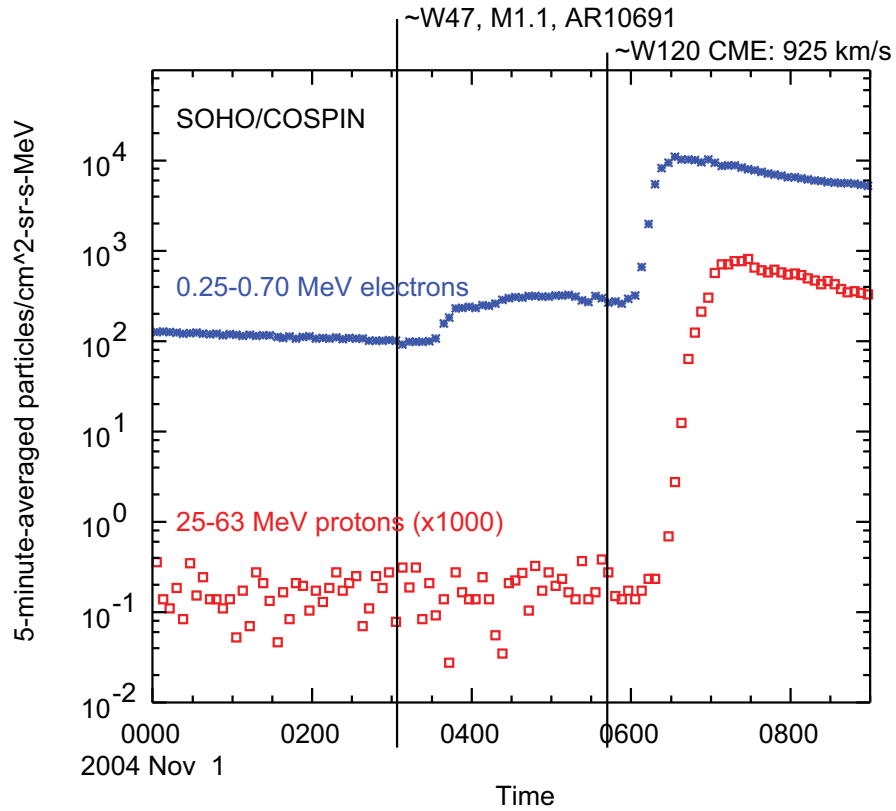| Interval No.	SEP Study Interval[a] Start Time (UT)	End Time (UT)	Onset Times (UT) Flare[b1]	SEP[b2]	Flare Size	Location	CME[c] PA	Speed	NOAA AR
1	1998/04/23 18:00	04/25 00:00	04/20 09:38	04/20 11:52	M1.4	S43W90[d]	284	1863	8202
2	1998/05/09 15:00	05/11 17:00	05/09 03:04	05/09 05:30	M7.7	S17W102	262	2331	8210
3	1998/06/04 12:00	06/06 12:00	06/04 01:58[e]	06/04 12:00	—-	N18W157[j]	halo	1802	8226
4	1998/06/16 22:00	06/17 21:00	06/16 18:03	06/16 21:30	M1.0	S21W108	341	1484	8232
5	1998/08/22 19:00	08/24 18:00	08/21 23:57[f]	08/22 08:30	M9.0	N32E46[f]	na	na	8307
6	1998/10/01 07:00	10/02 08:00	09/30 13:08	09/30 14:53	M2.8	N19W90	na	na	8340
7	1998/11/05 23:00	11/07 08:00	11/05 19:00	11/05 22:30	M8.4	N22W18	halo	1118	8375
8	2003/03/17 20:00	03/18 10:00	03/17 18:50	03/17 20:08	X1.5	S14W38	291	1020	10314
9	2003/03/18 14:00	03/20 04:00	03/18 11:51	03/18 14:23	X1.5	S14W46	263	1601	10314
10	2003/04/08 06:00	04/10 00:00	04/07 09:25	04/07 11:30	B7.3	S11W80	272	719	10324
11	2003/05/28 05:00	05/29 02:00	05/27 22:56	05/28 04:30	X1.3	S07W16	halo	964	10365
12	2003/05/31 04:00	06/01 23:00	05/31 02:13	05/31 03:38	M9.3	S07W59	halo	1835	10365
13	2003/06/18 09:00	06/21 00:00	06/17 22:27	06/18 08:38	M6.8	S08E58	halo	1813	10386
14	2004/11/01 07:00	11/01 23:00	11/01 <06:05[k]	11/01 06:54	—-	W120[g]	266	925	10684
15	2004/12/03 09:00	12/05 00:00	12/02 23:44	12/03 03:38[h]	M1.5	N07W01	halo	1216	10708
16	2005/01/15 07:00	01/15 20:00	01/15 05:54	01/15 07:08	M8.6	N15E00	halo	2049	10720
17	2005/01/16 00:00	01/16 11:00	01/15 22:25	01/15 23:54	X2.6	N14W08	halo	2861	10720
18	2005/06/17 19:00	06/18 10:00	06/16 20:01	06/16 21:24	M4.0	N08W89	na	na	10786
19	2005/07/18 23:00	07/20 10:00	07/17 11:20[g]	07/17 14:23	—-	NW120[g]	halo	1527	10786
20.1	2005/07/27 02:00	07/27 20:00	07/24 13:45[g]	07/25 19:08	—-	NE134	halo	2528	10792
20.2	2005/07/28 11:00	08/01 06:00	07/24 13:45[g]	07/25 19:08	—-	NE134	halo	2528	10792
21	2005/08/22 02:00	08/22 16:00	08/22 00:44	08/22 01:53	M2.6	S10W54	halo	1194	10798
22	2005/08/29 14:00	08/31 00:00	08/29 10:45	08/29 13:38	—-	W141	halo	1600	10798
23	2005/09/07 20:00	09/09 01:00	09/07 17:17	09/07 19:53	X17	S12E89	na	na	10808
24	2006/07/06 10:00	07/09 00:00	07/06 08:13	07/06 10:08	M2.5	S09W35	halo	911	10898

[a]Start and end time of SEP study intervals, rounded to the nearest hour. In some cases, these intervals do not encompass the whole SEP event due to our selection criteria (see text). Event 20 has been divided into two parts, reflecting a change in the IMF footpoint during the event.

[b1]Soft x-ray onset time from GOES or, for events behind the limb, type-III onset time from Wind/Waves.

[b2]SEP onset in Wind/EPACT, generally from background-subtracted ∼20 MeV protons; center of 15-minute-averaged bin.

[c]position angle and speed from http://cdaw.gsfc.nasa.gov/CME_list/. "na" denotes LASCO data gap.

[d]From Gopalswamy (2003).

[e]No flare seen. Likely backsided. Time are for the eruption observed by SOHO/EIT at the WNW limb.

[f]AR8307, based on Solar and Geophysical Activity Summary and Active Region Summary reports from National Weather Service Space Weather Prediction Center.

[g]From Cane et al. (2006).

[h]SEP onset time taken from ∼2 MeV protons observed by Wind/EPACT/LEMT.

[i]Based on the likely source in AR10759.

[j]Based on the likely source in AR8226, which was on the west limb at N18W91 at 2330 UT on 1998 May 29.

[k]Extrapolated from the observed first arrival of relativistic electrons, as reported by the Comprehensive Suprathermal and Energetic Particle Analyzer (COSTEP; Müller-Mellin et al. 1995) on SOHO).

Table 2.   Event and IMF Source Locations

Interval No.	Flare/CME Source[a]	IMF Footpoint at SS at Start[b]	IMF$_{SS}$[d]	IMF Footpoint at Sun[d] at Start[c]	at End[c]	Lat/Long[e]	IMF$_{Sun}$[d]	Nearby NOAA AR	IMF Source Type[f]
1	1934/11/-43	1935/297/-5	-75	1935/281/-35	1935/259/-28	S34W44	-67	—	Q-CH/PCH
2	1935/136/-17[g]	1935/70/-3	-66	1935/52/-21	1935/48/-21	S21W24	-79	8217	A-CH/AR1
3	1936/208/18	1936/103/0	-104	1936/89/-23	1936/69/-18	S23W44	-123	—	Q-CH/PCH
4	1937/351/-21[g]	1937/299/-1	-54	1937/330/-16	1937/320/-6	S16W89	-21	8232	A-CH/AR0
5	1939/41/32	1939/129/7	85	1939/104/21	1939/101/19	N21W28	57	8309	A-CH/AR1
6	1940/15/19	1941/322/7	-53	1941/296/-14	1941/286/-17	S14W21	-84	8349	A-CH/AR1
7	1942/184/22	1942/220/4	39	1942/213/16	1942/211/15	N16W49	28	—	Q-CH/EqCH
8	2000/62/-14	2000/53/-7	-11	2000/56/-25	2000/54/-24	S25W33	-12	10314	A-CH/AR0
9	2000/61/-14	2000/42/-7	-20	2000/52/-24	2000/46/-27	S24W38	-13	10314	A-CH/AR0
10	2001/192/-11	2001/156/-6	-36	2001/135/-15	2001/122/-14	S15W34	-56	10331	A-CH/AR1
11	2003/180/-7	2003/192/-1	13	2003/201/-14	2003/197/-13	S14W40	22	10365	A-CH/AR0
12	2003/182/-7	2003/151/-1	-31	2003/143/-14	2003/135/-16	S14W22	-39	10368	A-CH/AR1
13	2004/188/-8	2004/282/1	94	2004/258/-3	2004/252/-10	S03W17	70	—	Q-CH/EqCH
14	2022/214/-5[g]	2022/148/4	-67	2022/144/13	2022/144/13	N13W50	-72	10691	A-CH/AR1
15	2023/38/7	2023/86/1	48	2023/106/-4	2023/105/-4	S04W75	69	—	Q-CH/EqCH
16	2025/187/15	2025/221/-5	39	2025/244/16	2025/244/17	N16W58	55	—	Q-CH/PCH
17	2025/186/14	2025/218/-5	37	2025/244/17	2025/243/18	N17W68	56	—	Q-CH/PCH
18	2030/61/8	2030/0/1	-61	2030/37/-8	2030/37/-8	S08W77	-29	10776	A-CH/AR1
19	2031/48/11[g]	2032/323/5	-84	2032/290/3	2032/281/3	N03W23	-117	—	Q-CH/EqCH
20.1	2032/58/12[g]	2032/232/5	162	2032/224/-7	2032/223/-5	S07W64	165	—	Q-CH/EqCH
20.2	2032/58/12[g]	2032/181/6	121	2032/166/-5	2032/159/0	S05W24	109	—	Q-CH/EqCH
21	2033/231/-10	2033/221/7	-20	2033/232/-6	2033/232/-6	S06W56	4	10798	A-CH/AR0
22	2033/219/-9[g]	2033/136/7	-84	2033/152/18	2033/150/20	N18W75	-71	10800	A-CH/AR1
23	2034/227/-12[g]	2033/13/7	146	2033/37/-30	2033/25/-27	S30W82	137	—	Q-CH/PCH
24	2045/332/-9	2045/335/3	12	2045/343/0	2045/340/1	N00W47	14	10898	A-CH/AR0

[a]Carrington Rotation number/longitude/latitude based on the onset time and location of the flare (see Table 1).

[b]Carrington Rotation number/longitude/latitude at the Source Surface (SS, at 2.5 R$_\odot$).

[c]Carrington Rotation number/longitude/latitude based on the PFSS model (see text).

[d]Angular distance (in degrees) to the Flare/CME source location; IMF$_{SS}$: IMF footpoint at the Source Surface for Interval Start; IMF$_{Sun}$: IMF footpoint at the Sun for Interval Start; Sign: positive (negative)=IMF location at the west (east) side of the flare/CME source.

[e]Solar latitude and longitude of the IMF-footpoint at the start of the SEP interval.

[f]A-CH: An active-CH IMF-source with 'AR0' denoting that the nearby AR is the same one that is associated with the flare/CME that caused the SEP event, and with 'AR1' denoting that the nearby AR is a different AR. Q-CH: a quiet-CH IMF-source with 'EqCH' denoting an equatorial/low-latitude coronal hole, and 'PCH' denoting the low-latitude extension of a polar coronal hole.

[g]Based on the likely source in AR8210 (Event 2), AR8232 (Event 4), AR10684 (Event 14), AR10786 (Event 19), AR10792 (Event 20), AR10798 (Event 22), AR10808 (Event 23).

Table 3.   Interval-Averaged Fe/O Ratio at Various Energies

No.[a]	2.5-3.2 MeV/nuc[b]	3.2-5.0 MeV/nuc[b]	5-10 MeV/nuc[b]	10-15 MeV/nuc[c]	15.8-21.5 MeV/nuc[c]	21.5-36.3 MeV/nuc[c]	Source Type
1	0.114 ± 0.003	0.098 ± 0.002	0.046 ± 0.001	0.009 ± 0.001	0.006 ± 0.002	0.007 ± 0.005	Q-CH/PCH
2	0.210 ± 0.007	0.281 ± 0.007	0.326 ± 0.009	0.341 ± 0.017	0.309 ± 0.025	0.424 ± 0.038	A-CH/AR1
3	0.012 ± 0.004	0.017 ± 0.004	0.008 ± 0.003	<0.01[d]	0.032 ± 0.032	0.036 ± 0.037	Q-CH/PCH
4	0.020 ± 0.003	0.049 ± 0.006	0.087 ± 0.013	0.086 ± 0.032	0.053 ± 0.039	0.148 ± 0.090	A-CH/AR0
5	0.064 ± 0.002	0.079 ± 0.003	0.075 ± 0.003	0.075 ± 0.009	0.059 ± 0.017	0.090 ± 0.035	A-CH/AR1
6	0.056 ± 0.001	0.091 ± 0.002	0.115 ± 0.002	0.103 ± 0.004	0.138 ± 0.011	0.249 ± 0.027	A-CH/AR1
7	0.011 ± 0.001	0.019 ± 0.001	0.041 ± 0.005	0.146 ± 0.027	0.074 ± 0.045	0.068 ± 0.049	Q-CH/EqCH
8	0.446 ± 0.039	0.423 ± 0.034	0.367 ± 0.037	0.170 ± 0.044	0.289 ± 0.135	0.261 ± 0.166	A-CH/AR0
9	0.186 ± 0.018	0.156 ± 0.015	0.178 ± 0.020	0.176 ± 0.033	0.253 ± 0.070	0.091 ± 0.047	A-CH/AR0
10	0.021 ± 0.005	0.021 ± 0.005	0.009 ± 0.006	<0.05[d]	<1[d]	<0.3[d]	A-CH/AR1
11	0.072 ± 0.004	0.135 ± 0.006	0.230 ± 0.011	0.223 ± 0.014	0.213 ± 0.025	0.388 ± 0.048	A-CH/AR0
12	0.178 ± 0.005	0.203 ± 0.005	0.248 ± 0.009	0.359 ± 0.029	0.356 ± 0.056	0.456 ± 0.081	A-CH/AR1
13	0.035 ± 0.001	0.029 ± 0.001	0.021 ± 0.001	0.007 ± 0.002	0.011 ± 0.008	0.091 ± 0.066	Q-CH/EqCH
14	0.808 ± 0.049	0.741 ± 0.038	0.691 ± 0.037	0.356 ± 0.037	0.461 ± 0.069	0.416 ± 0.080	A-CH/AR1
15	0.035 ± 0.002	0.031 ± 0.002	0.026 ± 0.002	0.008 ± 0.002	0.004 ± 0.004	<0.03[d]	Q-CH/EqCH
16	0.086 ± 0.007	0.088 ± 0.007	0.120 ± 0.012	0.152 ± 0.031	0.181 ± 0.060	0.225 ± 0.092	Q-CH/PCH
17	0.032 ± 0.001	0.040 ± 0.002	0.073 ± 0.003	0.078 ± 0.003	0.063 ± 0.004	0.063 ± 0.006	Q-CH/PCH
18	0.129 ± 0.040	0.217 ± 0.046	0.371 ± 0.071	0.279 ± 0.072	0.235 ± 0.108	0.263 ± 0.144	A-CH/AR1
19	0.124 ± 0.008	0.093 ± 0.006	0.093 ± 0.008	0.061 ± 0.016	0.039 ± 0.028	0.042 ± 0.043	Q-CH/EqCH
20.1	0.214 ± 0.022	0.173 ± 0.013	0.105 ± 0.007	0.034 ± 0.006	0.020 ± 0.007	0.052 ± 0.018	Q-CH/EqCH
20.2	0.072 ± 0.001	0.060 ± 0.001	0.045 ± 0.001	0.020 ± 0.001	0.012 ± 0.002	0.017 ± 0.004	Q-CH/EqCH
21	0.223 ± 0.016	0.219 ± 0.013	0.241 ± 0.016	0.171 ± 0.019	0.122 ± 0.028	0.286 ± 0.064	A-CH/AR0
22	0.076 ± 0.012	0.080 ± 0.011	0.076 ± 0.014	0.152 ± 0.037	0.139 ± 0.056	0.132 ± 0.069	A-CH/AR1
23	0.048 ± 0.002	0.034 ± 0.001	0.034 ± 0.001	0.066 ± 0.003	0.117 ± 0.005	0.175 ± 0.006	Q-CH/PCH
24	0.166 ± 0.011	0.141 ± 0.009	0.161 ± 0.012	0.134 ± 0.022	0.132 ± 0.041	0.157 ± 0.059	A-CH/AR0

[a]Interval reference number, from Table 1

[b]from Wind/EPACT/LEMT

[c]from ACE/SIS

[d]Upper limit based on one Fe ion

Table 4. Interval-Averaged Elemental Ratios at 5-10 MeV/nucleon[a]

No.[b]	C/O	Ne/O	Mg/O	Si/O	S/O	Ar/O	Ca/O	Source Type
1	0.461 ± 0.005	0.098 ± 0.002	0.205 ± 0.003	0.118 ± 0.002	0.018 ± 0.001	0.0018 ± 0.0002	0.0053 ± 0.0004	Q-CH/PCH
2	0.381 ± 0.010	0.247 ± 0.007	0.259 ± 0.007	0.191 ± 0.006	0.038 ± 0.003	0.0097 ± 0.0013	0.0214 ± 0.0019	A-CH/AR1
3	0.516 ± 0.035	0.138 ± 0.014	0.137 ± 0.015	0.040 ± 0.008	0.008 ± 0.003	0.0040 ± 0.0023	0.0013 ± 0.0013	Q-CH/PCH
4	0.348 ± 0.032	0.125 ± 0.016	0.178 ± 0.020	0.138 ± 0.017	0.006 ± 0.003	<0.0019[c]	0.0057 ± 0.0033	A-CH/AR0
5	0.507 ± 0.011	0.141 ± 0.004	0.174 ± 0.005	0.100 ± 0.004	0.016 ± 0.001	0.0027 ± 0.0006	0.0081 ± 0.0010	A-CH/AR1
6	0.471 ± 0.006	0.149 ± 0.003	0.207 ± 0.003	0.122 ± 0.003	0.020 ± 0.001	0.0031 ± 0.0004	0.0115 ± 0.0007	A-CH/AR1
7	0.645 ± 0.027	0.141 ± 0.010	0.179 ± 0.011	0.070 ± 0.007	0.009 ± 0.002	0.0030 ± 0.0013	0.0041 ± 0.0016	Q-CH/EqCH
8	0.386 ± 0.040	0.346 ± 0.035	0.430 ± 0.041	0.143 ± 0.021	0.037 ± 0.010	0.0208 ± 0.0075	0.0521 ± 0.0120	A-CH/AR0
9	0.397 ± 0.034	0.208 ± 0.021	0.209 ± 0.022	0.171 ± 0.019	0.022 ± 0.006	0.0090 ± 0.0041	0.0198 ± 0.0060	A-CH/AR0
10	0.594 ± 0.068	0.066 ± 0.017	0.104 ± 0.023	0.061 ± 0.017	0.004 ± 0.004	<0.0044[c]	0.0087 ± 0.0062	A-CH/AR1
11	0.495 ± 0.019	0.218 ± 0.011	0.253 ± 0.012	0.150 ± 0.009	0.023 ± 0.003	0.0072 ± 0.0018	0.0217 ± 0.0031	A-CH/AR0
12	0.412 ± 0.013	0.220 ± 0.008	0.217 ± 0.008	0.131 ± 0.006	0.019 ± 0.002	0.0114 ± 0.0017	0.0227 ± 0.0024	A-CH/AR1
13	0.615 ± 0.007	0.115 ± 0.002	0.179 ± 0.003	0.070 ± 0.002	0.009 ± 0.001	0.0005 ± 0.0002	0.0029 ± 0.0004	Q-CH/EqCH
14	0.357 ± 0.025	0.194 ± 0.016	0.245 ± 0.019	0.239 ± 0.019	0.059 ± 0.008	0.0159 ± 0.0043	0.0431 ± 0.0072	A-CH/AR1
15	0.438 ± 0.011	0.095 ± 0.004	0.201 ± 0.006	0.074 ± 0.004	0.008 ± 0.001	0.0008 ± 0.0004	0.0028 ± 0.0007	Q-CH/EqCH
16	0.380 ± 0.024	0.132 ± 0.012	0.189 ± 0.015	0.117 ± 0.011	0.021 ± 0.005	0.0079 ± 0.0028	0.0049 ± 0.0022	Q-CH/PCH
17	0.417 ± 0.008	0.147 ± 0.004	0.181 ± 0.005	0.107 ± 0.003	0.017 ± 0.001	0.0027 ± 0.0005	0.0064 ± 0.0008	Q-CH/PCH
18	0.459 ± 0.085	0.109 ± 0.033	0.190 ± 0.047	0.095 ± 0.032	0.038 ± 0.019	<0.0095[c]	0.0190 ± 0.0136	A-CH/AR1
19	0.402 ± 0.021	0.170 ± 0.012	0.191 ± 0.013	0.122 ± 0.010	0.022 ± 0.004	0.0042 ± 0.0017	0.0097 ± 0.0026	Q-CH/EqCH
20.1	0.396 ± 0.016	0.108 ± 0.007	0.191 ± 0.010	0.138 ± 0.008	0.028 ± 0.003	0.0024 ± 0.0010	0.0104 ± 0.0021	Q-CH/EqCH
20.2	0.518 ± 0.004	0.118 ± 0.001	0.184 ± 0.002	0.101 ± 0.001	0.016 ± 0.001	0.0030 ± 0.0002	0.0055 ± 0.0003	Q-CH/EqCH
21	0.302 ± 0.019	0.163 ± 0.012	0.153 ± 0.012	0.107 ± 0.010	0.028 ± 0.005	0.0071 ± 0.0024	0.0206 ± 0.0041	A-CH/AR0
22	0.432 ± 0.039	0.169 ± 0.021	0.111 ± 0.017	0.079 ± 0.014	0.018 ± 0.006	0.0044 ± 0.0031	0.0175 ± 0.0062	A-CH/AR1
23	0.545 ± 0.007	0.158 ± 0.003	0.126 ± 0.003	0.070 ± 0.002	0.014 ± 0.001	0.0024 ± 0.0003	0.0032 ± 0.0004	Q-CH/PCH
24	0.322 ± 0.020	0.150 ± 0.012	0.188 ± 0.013	0.132 ± 0.011	0.033 ± 0.005	0.0048 ± 0.0020	0.0063 ± 0.0023	A-CH/AR0

[a]from Wind/EPACT/LEMT. See Table 3 for Fe/O.

[b]Interval reference number, from Table 1

[c]Upper limit based on one Ar ion

Table A1. 1998, 2003-2006 SEP Events with Successful Field-Line Tracing

Event No.	SEP Event Interval Start Time (UT)	End Time (UT)	Wind/LEMT 3-10 MeV/n Fe/O [a]	Z(>34)/O [a]	ACE/ULEIS 0.32-0.64 MeV/n ^{3}He/^{4}He [b]	GOES[e] >10 MeV p/cm^2-sr-s	SOHO/COSTEP[e] 0.25-0.70 MeV e/cm^2-sr-s	electron/proton (e/p) Ratio [f]
1	1998/04/20 12:00	1998/04/25 00:00	1.35 ± 0.01	2.2 ± 0.2	< 2.5%	1.54E+03	1.85E+05	120
2	1998/05/09 06:00	1998/05/11 17:00	2.42 ± 0.04	5.5 $^{+7.2}_{-3.6}$	< 2.2%	1.06E+01	9.86E+02	93
3	1998/06/04 06:00	1998/06/06 12:00	0.11 ± 0.02	< 24	< 2.7%	8.06E-01	9.32E+00	12
4	1998/06/16 22:00	1998/06/19 00:00	0.75 ± 0.04	< 9.0	< 1.5%	1.74E+00	9.90E+01	57
5	1998/08/22 09:00	1998/08/24 18:00	0.67 ± 0.02	< 1.9	< 0.9%	2.67E+00	2.85E+02[d]	107
6	1998/09/30 15:00	1998/10/03 00:00	1.86 ± 0.01	2.4 ± 0.5	< 1.5%	9.79E+02	2.75E+04[d]	28
7	1998/11/05 23:00	1998/11/07 08:00	0.19 ± 0.01	3.5 $^{+8.0}_{-2.9}$	< 1.1%	6.65E+00	2.92E+01	4
8	2003/03/17 20:00	2003/03/18 10:00	3.27 ± 0.21	< 45	< 3.0% [c]	7.00E-01	4.14E+02	591
9	2003/03/18 14:00	2003/03/20 04:00	1.36 ± 0.10	< 30	< 0.9%	4.62E-01	2.03E+03	4393
10	2003/04/07 12:00	2003/04/10 00:00	0.16 ± 0.03	< 27	< 0.9%	6.84E-01	6.03E+02	882
11	2003/05/28 05:00	2003/05/30 09:00	1.63 ± 0.02	1.1 $^{+1.4}_{-0.7}$	< 0.7%	9.43E+01	1.73E+03	18
12	2003/05/31 04:00	2003/06/01 23:00	1.84 ± 0.04	< 3.0	< 0.8%	2.53E+01	1.33E+04	526
13	2003/06/18 08:00	2003/06/21 00:00	0.22 ± 0.01	< 0.6	< 0.8%	1.38E+01	1.97E+03	143
I1	2004/10/30 03:00	2004/11/01 03:00	5.61 ± 0.11	52 $^{+24}_{-17}$	6.0±0.2%	1.87E+00	2.80E+03	1499
14	2004/11/01 06:00	2004/11/03 00:00	5.52 ± 0.18	16 $^{+37}_{-14}$	< 5.8% [c]	5.45E+01	3.56E+03	65
15	2004/12/03 09:00	2004/12/05 06:00	0.24 ± 0.01	< 2.1	< 0.8%	1.97E+00	3.27E+02	166
16	2005/01/15 07:00	2005/01/15 23:00	0.86 ± 0.05	< 11	< 1.1%	7.59E+00	3.72E+02	49
17	2005/01/16 00:00	2005/01/17 12:00	0.74 ± 0.01	0.7 $^{+0.6}_{-0.4}$	< 0.8%	3.33E+02	1.23E+04	37
I2	2005/05/06 00:00	2005/05/07 15:00	5.13 ± 0.09	85 $^{+22}_{-17}$	< 1.4%	2.05E+00	5.54E+02	270
18	2005/06/16 22:00	2005/06/19 00:00	2.31 ± 0.11	< 22	< 1.7%	4.13E+01	6.26E+03	151
19	2005/07/17 16:00	2005/07/20 10:00	0.97 ± 0.02	< 1.7	< 1.3%	1.92E+01	2.13E+03	111
20	2005/07/25 19:00	2005/08/02 00:00	0.46 ± 0.01	< 0.2	< 1.2%	3.79E+01	1.01E+04	266
21	2005/08/22 02:00	2005/08/22 18:00	1.75 ± 0.07	< 12	< 0.9%	5.63E+00	1.56E+03	277
22	2005/08/29 14:00	2005/08/31 06:00	0.70 ± 0.07	< 29	< 1.5%	1.07E+00	2.56E+02	239
23	2005/09/07 20:00	2005/09/12 04:00	0.40 ± 0.01	0.3 $^{+0.3}_{-0.2}$	< 0.9%	1.01E+03	1.62E+05	160
24	2006/07/06 10:00	2006/07/10 00:00	1.25 ± 0.06	< 12	< 1.2%	1.84E+00	3.19E+01	17

[a]Normalized to the nominal coronal ratios, Fe/O = 0.134 (Reames 1995) and Z(>34)/O = 2.66 × 10^{-5} (Reames 2000). Upper limits correspond to one Z(>34) ion. Asymmetric error bars use Poisson statistics, as given by Gehrels (1986).

[b]95% confidence-level upper limits.

[c]Upper limit includes residual ^{3}He from the decay phase of preceding impulsive events.

[d]These events occurred during a SOHO data gap. Electron intensity is estimated from simultaneous ACE/EPAM data, using equation (1) from Cliver & Ling (2007).

[e]Peak hourly-averaged intensity. Read 1.54E+03 as 1.54 × 10^3.

[f]This empirical e/p ratio is based on the datasets and methods used in Cliver & Ling (2007).

Table A2.   Soft X-Ray (SXR) Flares & CMEs Associated with Impulsive Events I1 and I2

| Date | SXR Flare Times (UT) | | | SXR Duration (minutes) | SXR Class | SXR Location | NOAA Active Region | Speed (km/s) | Associated CME [a] Launch Time (UT) | | width (degrees) |
	Start	Maximum	End						[b]	[c]	
2004/10/30	0039	0049	0053	14	C9.7	N14W13	10691	424	2328[d]	2343[d]	19
2004/10/30	0323	0333	0337	14	M3.3	N14W15	10691	—	—	—	—
2004/10/30	0608	0618	0622	14	M4.2	N14W21	10691	422	0609	0448	Halo
2004/10/30	0909	0928	0930	21	M3.7	N15W23	10691	552	0903	0936	74
2004/10/30	1138	1146	1150	12	X1.2	N12W18	10691	427	1142	1146	Halo
2004/10/30	1618	1633	1637	19	M5.9	N15W20	10691	690	1609	1632	Halo
2004/10/31	0523	0532	0539	17	M2.3	N13W34	10691	265	0507	0439	62
2004/11/01	0304	0322	0326	22	M1.1	∼W47	10691	459	0259	0305	>192
2005/05/04	0148	0154	0203	15	B5.3	S10W41	10756 [e]	278	0211	0151	17
2005/05/04	1315	1320	1323	8	B6.4	∼W48	10756 [e]	634	1328	1328	86
2005/05/05	1435	1440	1455	20	C2.4	∼W57	10756 [e]	—	—	—	—
2005/05/05	2009	2020	2027	18	C7.8	S03W65	10756 [f]	427	1935	1953	52
2005/05/06	0305	0314	0321	16	C9.3	S04W71	10756	1120	0254	0255	109
2005/05/06	1111	1128	1135	24	M1.3	S04W76	10756	1144	1102	1111	129

[a]From the SOHO/LASCO CME catalogue at http://cdaw.gsfc.nasa.gov/CME_list/.

[b]Based on a linear fit to LASCO height-time profile.

[c]Based on a quadratic fit to LASCO height-time profile.

[d]On previous day, 2004/10/29.

[e]SOHO/EIT movies showed transient activities also occurring at AR 10758 at the time of this flare. However, the magnetic field at L1 at the time of this flare (and the corresponding electron event, as shown in Figure A2) had positive polarity, in agreement with the field emerging from near AR 10756. The field emerging from near AR 10758, on the other hand, had negative polarity. Flaring activity at AR 10758 is thus inconsistent with being the origin of the observed solar energetic electrons.

[f]An 1180-km/s halo CME launched at ∼2013 UT. SOHO/EIT observation of post-flare loops indicate that the source of this CME was AR 10759, which was located behind the east limb at ∼E110 at this time.